T-1902

ARA DIVISION

GPO PRICE $ _____

CFSTI PRICE(S) $ _____

Hard copy (HC) 3.00

Microfiche (MF) .75

ff 653 July 65

FACILITY FORM 602

N67 12048 (ACCESSION NUMBER) | (THRU)

59 (PAGES) | 1 (CODE)

CR-80060 (NASA CR OR TMX OR AD NUMBER) | 32 (CATEGORY)

ALLIED RESEARCH ASSOCIATES, INC.
VIRGINIA ROAD · CONCORD, MASSACHUSETTS

PHOTOMECHANICAL INVESTIGATION OF STRUCTURAL BEHAVIOR OF GYROSCOPE COMPONENTS

TASK IV
ANALYSIS OF INITIAL REDESIGN OF AB5-K8 GYROSCOPE

Final Technical Report No. ARA 284-8

April 1966

H. Becker
F. F. Bird
P. E. Kyle
R. Papirno
C. N. Tang

Prepared For

NAS8-11294

Astrionics Laboratory
National Aeronautics and Space Administration
Huntsville, Alabama

ALLIED RESEARCH ASSOCIATES, INC
VIRGINIA ROAD • CONCORD, MASSACHUSETTS

SUMMARY

Theoretical and experimental investigations were conducted on the structure and the materials of the first of several redesigns of the AB5-K8 gyro. Shock and temperature loads were considered, and determination was made of the precision elastic limit (PEL) of the beryllium now being used in the gyro.

As a result of the investigations, elementary beam theory was shown to be a reliable procedure for predicting shaft deflections, a simple method of transient heat transfer was shown to have promise in shaft design, and an efficient fork configuration appeared to be achievable using thin, flat members cantilevered from the cover plate. The PEL of S-100 beryllium was at the low end of the range of properties of standard beryllium metal, below that of the high PEL beryllium (I-400), and far below what might be expected of steels.

TABLE OF CONTENTS

LIST OF FIGURES

SYMBOLS

a	Coefficient used in Eq. (21)
A	Area, sq. ft., also coefficient used in Eq. (21)
A_1	Area of contact surface between stator and shaft, sq. ft.
A_2	Area of contact surface between shaft and gas bearing, sq. ft.
b	Width of fork, in., also coefficient used in Eq. (21)
b_o	Initial width of fork, in.
c	Subscript for clamp
c_1, c_2	Specific heat for iron and beryllium respectively, btu/lb/F
C	The dimensionless number referred to in the theory of models
E	Young's modulus of elasticity, Msi (= 10^6 psi)
f	Subscript for fork, also fringe value of photomechanical material, psi-in/fringe
F	Force or applied load, lb.
F_o	Initial load, lb.
g	Gravitational acceleration, in/sec^2
h	Thickness of fork, also height of fork, in.
h_o	Initial thickness of fork, in.
H	Height of fork, in.
i	Indexing number
I	Moment of inertia, in^4
I_o	Moment of inertia of shaft cross section at a selected location, in^4
I_1, I_2	Moments of inertia corresponding to shaft segments 1 and 4 respectively, in^4
I_i, I_n	Moments of inertia of shaft cross section of segments i and n respectively, in^4
k_1, k_2	Thermal conductivity for iron and beryllium respectively, btu/hr/ft/F
ℓ_1	The total length of shaft segments 1 and 2, in.
ℓ_2	The total length of shaft segments 3 and 4, in.
L	Length in general, also over-all length of shaft, in. or ft.
L_1, L_2, L_3, L_4	Lengths of shaft segments 1, 2, 3, and 4 respectively, in.
L_n	Length of shaft segment n, in.

m	Mass, lb. $sec^2/in.$, also subscript for moment or model
M	Moment in general, also moment at shaft end and internal moment in shaft, in-lb.
n	Points in the shaft where change in cross section occurs, also the photomechanical fringe order, also the indexing number
p	Subscript for thrust in shaft, also subscript for prototype
P	Internal axial force or thrust in shaft, lb.
PEL	Precision elastic limit, psi.
q_1, q_2	Heat flow from stator to shaft and shaft to gas bearing respectively, btu/hr.
Q	Input heat, btu/hr.
s	Subscript for shear, also for shaft, also a coefficient used in Eq. (23)
sh	Subscript for shaft
S	Shear force, lb.
t	Time, seconds, minutes or hours, also thickness of photomechanical model, in.
T	Temperature, F, also torque, in. lb.
T_1, T_2	Temperatures in stator and
V_1, V_2	Volumes of stator and shaft respectively, ft^3
W	Total weight of rotor, stator and shaft, lb.
W_1, W_2	Weights of shaft segments 1 and 2 respectively, lb.
x	x coordinates, in.
y	Lateral deflection of shaft, in.
y_n	Lateral deflection of shaft at point n, in.
y_{m+p}	Maximum lateral deflection of shaft due to end moments and thrust, in.
y_m	Maximum lateral deflection of shaft due to end moments, in.
ΔT	Differences in temperature, F
δ	Lateral deflection of shaft, in.
δ_n	Lateral deflection of shaft at point n, in.
δ_m, δ_s	Movements at the center of shaft due to unit moment and shear respectively, in.
δ_p	Movement at the center of shaft due to unit thrust, in.
ϵ	Strain
θ	Slope of deflection curve of shaft or angle of twist of fork per unit length, radians/in.

ρ_1, ρ_2	Densities of iron and beryllium respectively, lbs/ft^3
σ	Stress, psi
σ_{tu}	Ultimare stress in tension, psi
σ_{ty}	Yield stress in tension, psi

INTRODUCTION

A. Scope of Investigation

The AB5-K8 gyroscope is in the process of design improvement by the Astrionics Laboratory. ARA is participating in this task by conducting structural investigations of several possible design configurations. This report describes the results of studies on the first of these designs.

There are four fundamental aspects to each design of the current ARA investigations:

1. Transient temperature analysis to determine the magnitudes of transient temperature differences which occur during start-up and shut-down of the gyro. Consider microcreep for cycling effects using transient heat transfer analysis with power/time data for gyro starting cycle.

2. Calculate shaft motions considering shaft shoulder details, bearing race movements, and thermal stresses and deformations arising from each component of the temperature distribution.

3. Photoelastic determination of cover stresses. Assume hot shaft and cool cover. Employ photothermoelastic procedures to evaluate shaft cover interaction.

4. Perform materials analysis to identify factors which may cause objectionable dimensional changes and/or distortions. To be considered are specific treatments of the materials during manufacture, choice of materials, and the operating environment.

The studies on the first design have focussed on four types of structures problems:

1. Shaft analysis optimization,
2. Fork geometry optimization,
3. A simplified transient temperature analyses,
4. Materials evaluation for microplasticity behavior.

All were investigated and are discussed in subsequent sections of this report.

SHAFT INVESTIGATION

A. Introduction

An important feature of the gyro structural design is the need for an accurate procedure to predict theoretically the deformation of a shaft. Because of the changes in section, there may be some question as to the degree of precision required in a mathematical model to achieve this goal.

In order to establish the proper model, a preliminary study was made of the current S-100 shaft design using elementary beam theory and photoelastic modeling. The influence of axial load on lateral deflection also was considered. As the data indicate, elementary beam theory should satisfy the needs of the gyro structural investigations. In addition, the photoelastic studies have highlighted possible problem areas.

B. Theory

1. Deflection Calculation

The analysis of the lateral deflection of the shaft is simplified by the fact that it is in symmetry, so that each half functions as a cantilever beam sprung from the transverse centerline. The mathematical model is shown in Fig. 1. The bearing seats are assumed to be structurally ineffective and are thus not included in the model. The two transverse holes in the actual shaft are not considered to influence the lateral deflection. Therefore, they are missing from the mathematical model. The thrust in the shaft is shown below to exert a negligible influence.

Thus, the governing equation for the model becomes

$$M/EI_n = d^2y/dx^2 \tag{1}$$

for segment n where n=1, 2, 3 and 4. Integrating this equation leads to the following expression for the lateral deflection at point n (Fig. 1).

$$y_n = y_{n-1} + L_n (dy/dx)_{n-1} + \delta_n \tag{2}$$

where

$$\delta_n = (M/2EI_n)(L_n)^2$$

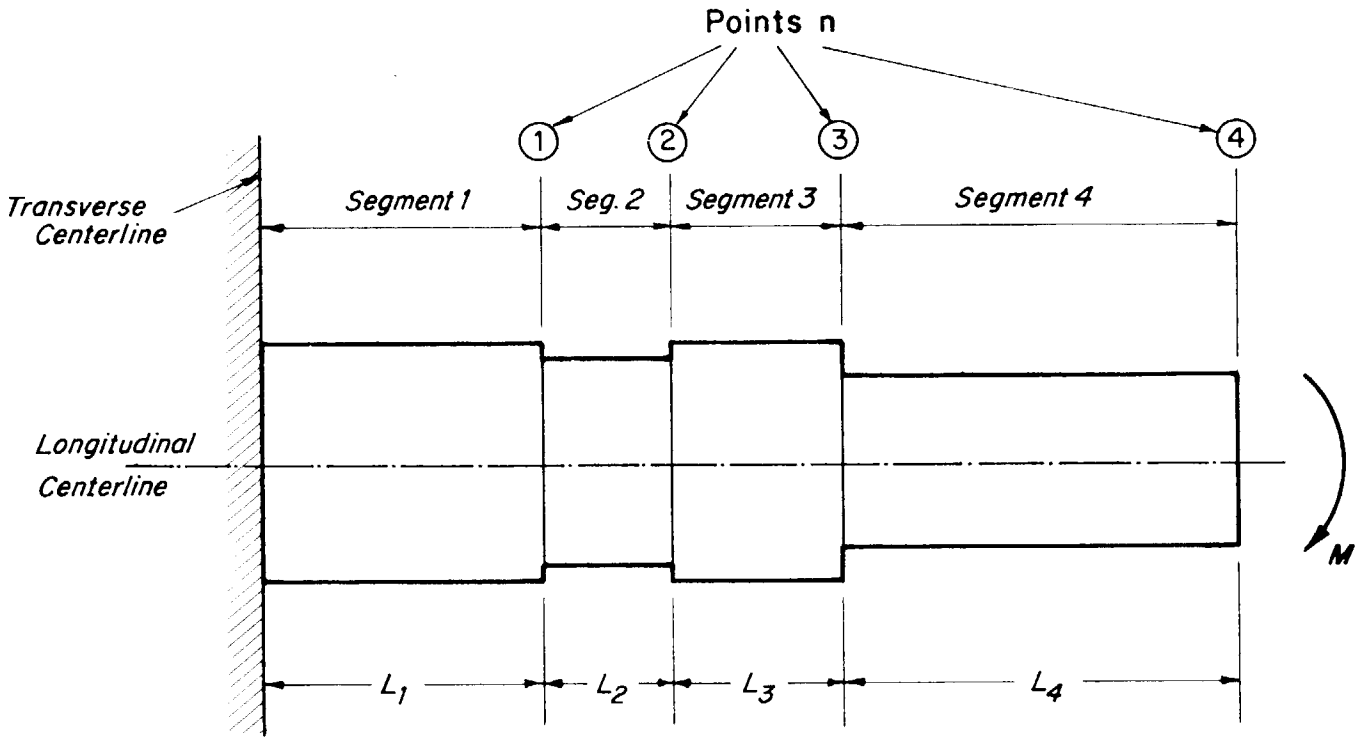

Figure 1 Basis for Mathematical Model of Shaft. (Sketch Not to Scale)

$$(dy/dx)_{n-1} = \Sigma\theta_i \qquad (i = 1, 2, 3, 4)$$

$$\theta_i = (M/EI_i)(L_i)$$

Eq. (2) was used to compute the lateral deflection of the shaft. The result is shown in Fig. 2 for the shaft shown in Astrionics Drawing GC 425661.

2. Influence of Axial Force

The possible influence of the thrust on computed deflections was estimated on the conservative assumption of constant shaft diameter at the smallest value, which occurs at each end. For such a shaft under the combined end moment and thrust, the influence of thrust can be seen from Table 1 where y_{m+p} represents the maximum lateral deflection caused by both moment and thrust, while y_m is the maximum deflection caused by moment only.

Table 1

Effect of Thrust on Shaft Lateral Deflection Under End Moments

Thrust* lbs.	kg	y_{m+p}/y_m**
30	13.6	1.004
100	45.4	1.013
300	136.0	1.040
500	227.0	1.073

*The expected value of the thrust in the actual shaft is below 10 lb. as computed from equations and data in Ref. 1.

**These values are taken from Ref. 2.

It is seen from this table that for a thrust as much as 10 times as large as would be expected, the additional deflection of such a shaft would be only about one percent over the pure moment deflection.

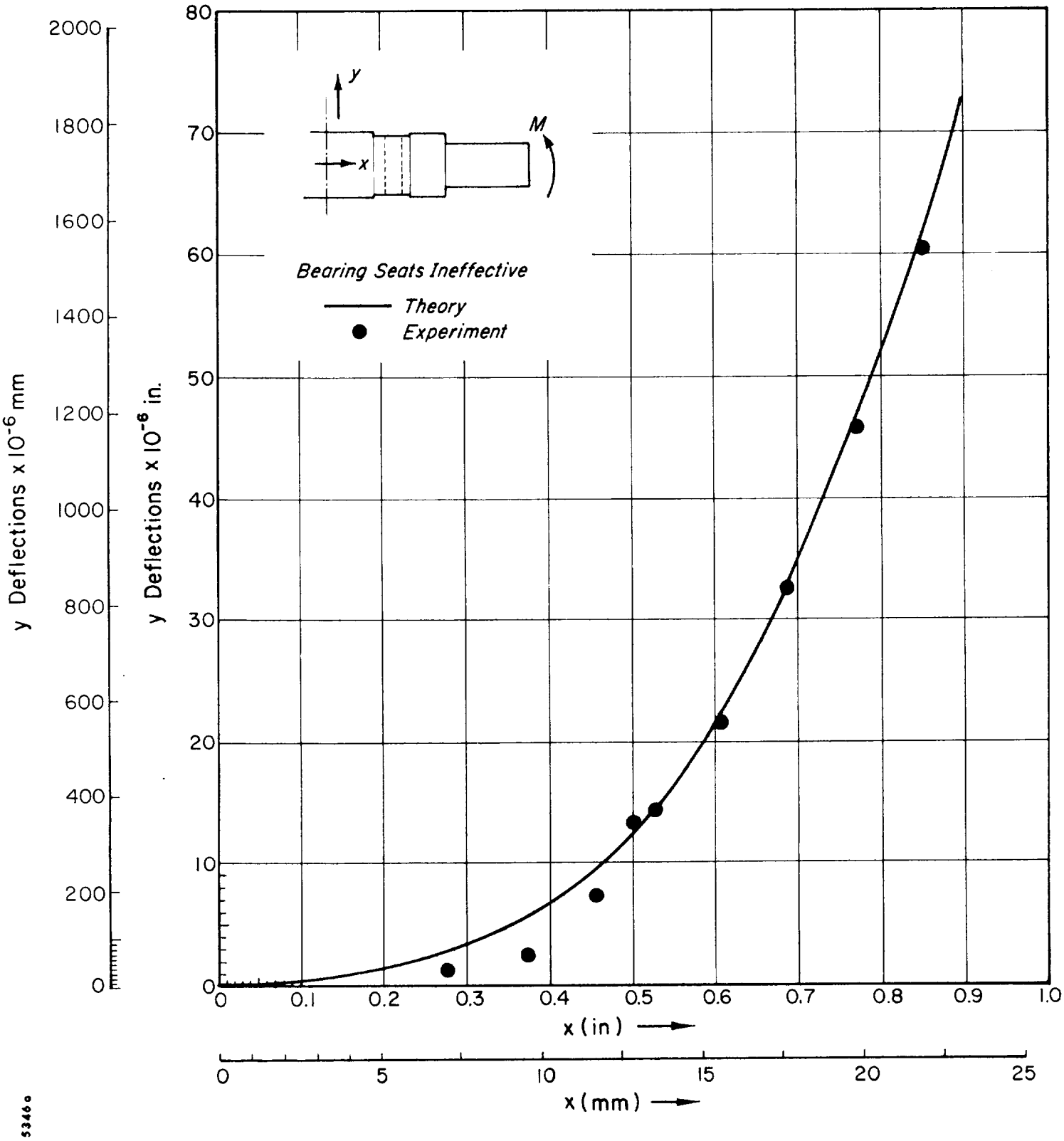

Figure 2 Comparison of Theory and Experiment for S-100 Beryllium Shaft

Just as the presence of thrust tends to increase lateral deflection, axial tension tends to reduce it. Consequently, it is apparent that any possible benefit of shaft tension would be negligibly small.

C. Experiments

1. Background

The intent of the experimental program was to obtain data to check and support the theoretical predictions of the lateral deformations of the gyroscope shaft. Measurements were made on a model of the shaft and were related to deformations predicted for the prototype shaft through modeling laws. In addition, photoelastic information was obtained concerning the stresses developed in the shaft. This information helped to understand the observed deformation and to direct further experimental effort in the detailed examinations of the stress concentrations developed at the diameter transitions along the prototype shaft.

2. The Stress Freezing Technique

In most photoelastic investigations loads are applied at room temperature to scaled models and the resulting deflections and photoelastic fringe patterns are recorded. However, this would be limited to two-dimensional analysis, for the most part. Analysis of stresses in a three-dimensional model (the gyro shaft, for example) is conducted effectively by a process known as stress freezing in which both deformations and fringe patterns are made available in slices cut from the model.

Normally, photoelastic epoxies (in this case Type 4290 Hysol) have a Young's modulus of about 450,000 psi (3100 n/mm^2) at 70 F (294 K). If the temperature of the material is raised to approximately 300 F (422 K) the modulus has a value of approximately 2,300 psi (16 n/mm^2). If loads are applied to the model at this higher temperature, deformations take place in relation to the lower modulus, and, if the loads are held constant and the model is cooled to room temperature, these deformations will remain after load has been removed and the modulus has now returned to the room temperature value of 450,000 psi (3100 n/mm^2).

In addition to the deflection, the plastic will retain photoelastic fringe patterns that obey the stress-optic law, $n = \sigma t/f$, with the calibrated fringe order constant associated with the elevated temperature. The deformations and photoelastic fringe patterns are frozen into the plastic model and slicing the model has no influence upon the deformations or fringe patterns. As a result, the three-dimensional behavior is easily observable in plane slices.

3. Modeling Law

A structural modeling law is most effective when it relates the quantity of interest to structural properties in a simple manner. In the case of the moment loaded shaft the quantity of interest is deflection and the structural properties are shaft geometry and Young's modulus. Consequently, it would be appropriate to begin with the elementary relation for deflection of the tip of a uniform cantilever beam.

$$\delta = (1/2)ML^2/EI \tag{3}$$

For a beam of lengthwise variable section, the factor (1/2) becomes a coefficient C which depends upon the manner in which the section varies from some reference value I_o at a selected location such as the root

$$\delta = CML^2/EI_o \tag{4}$$

It is a fundamental principle of elasticity that in a homogeneous structure stresses are a function of geometry only and deformations are proportional to Young's modulus. This means that the coefficient C would be the same for model and prototype, independent of scale and material, which permits the modeling law to be written in ratio form

$$(EI_o\delta/ML^2)_m = (EI_o\delta/ML^2)_p \tag{5}$$

This was the relation used to convert the photoelastic model shaft deflections (E = 2.3 ksi)(16 n/mm^2) to those of the prototype beryllium shaft (E = 42 Msi), (29 x 10^4 n/mm^2).

4. Model Fabrication

Plastic models of the gyroscope shaft were machined from plastic stock at six times full size of Drawing GC 425661. During the process of machining, the models were annealed at 300 F (422 K) to assure that no residual stresses remained in the finished model. The bearing collars were machined from the same material as the shaft (Hysol 4290) and were fitted to the 6X dimensions at the maximum interference on the shaft. The collar on one end of the model was pressed on in an arbor press in the conventional way. The collar for the other end was put on by cooling the shaft and slipping the collar onto the shaft with no interference present.

The shaft was then allowed to warm to room temperature. The purpose in this assembly procedure was to see if there was a detectable difference in the performance of the collar depending upon which assembly procedure was used. No difference was, in fact, detected.

Short, solid bars of epoxy were cemented to the ends of the shafts for the purpose of applying the bending moments to each end. A finished shaft is shown in Fig. 3. A finished shaft with the end bars and the collars in place is shown in Fig. 4.

5. Stress Freezing Under Load

In certain cases, one of the precautions that must be taken during stress freezing is to compensate the model for deflections and stresses caused by the weight of the model itself. As an example of this effect, assume that the shaft model were lying on a surface with the smaller diameter shaft stubs unsupported. Assume also that the solid attachment of the shaft extensions has not yet been made. A previous calculation on the shaft showed that 1.64 inch pounds (185 mm n) of torque applied to each end would produce adequate deflections during stress freeze. Using 0.04 lb/in^3 as the density of the plastic, the bending moment produced at the root of the stub shaft where it joins the center section is nearly 10% of the applied moment. This would produce an intolerable experimental error.

This effect was reduced to an acceptable amount by the technique outlined in Fig. 5. In this scheme, the support wires picked up the weight of the model at evenly spaced locations along the model length reducing the error to about 1% of the applied moment. Fig. 5 shows a sketch of the shaft with the support wires in position and moment being applied to the extension by transverse forces F.

Fig. 6 shows the complete counter-balancing jig with a shaft in place. The jig and shaft assembly were placed in the oven for the stress freeze cycle after which the model was removed for analysis.

6. Deflection Analysis

The profile of the deflected beam was measured with standard machine tool techniques on a granite surface plate to a precision of better than 0.0005 inch (0.0127 mm). This implies a precision of about $\pm$ 1% of the tip deflection since the actual total deflection from the center of the shaft to the tip of the stub shaft was about 0.050 inch (1.27 mm).

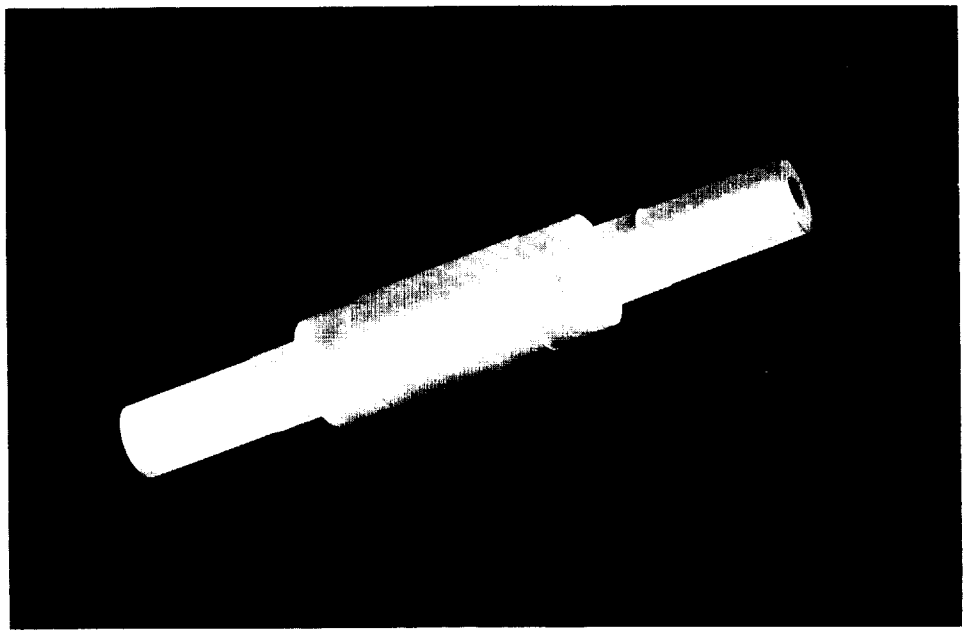

Figure 3 Shaft Before Attachment of Moment Bars

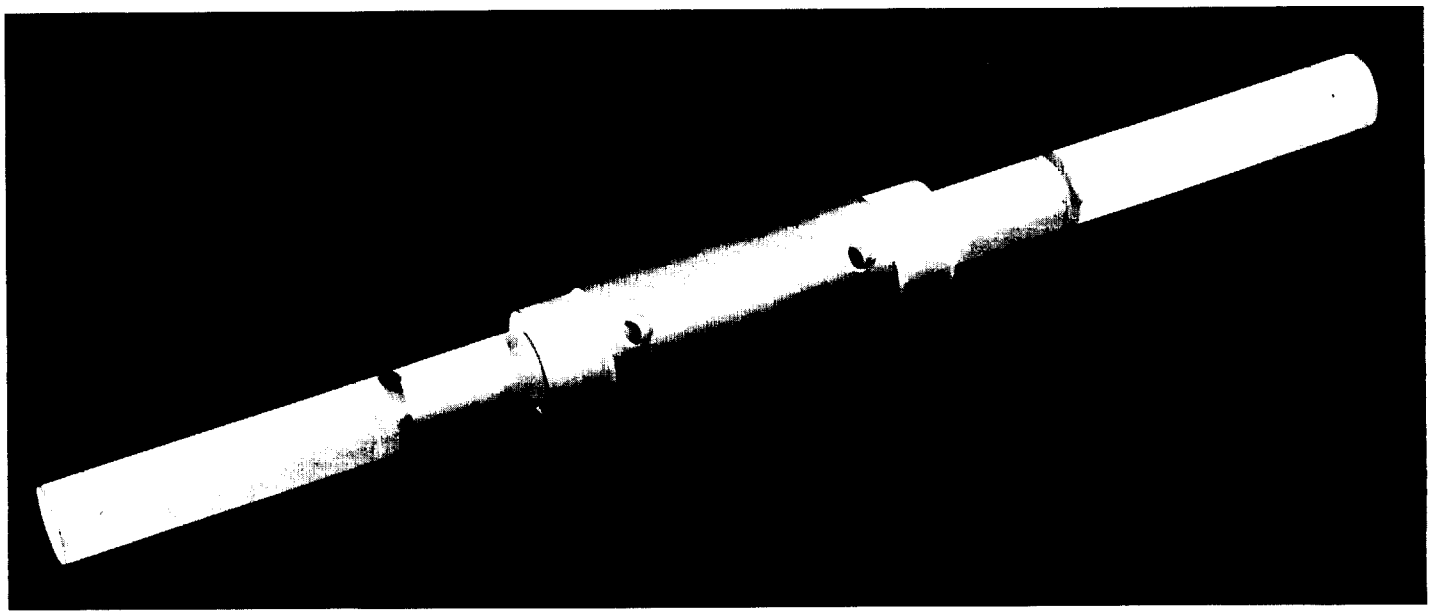

Figure 4 Shaft With Bearing Collars and Moment Bars Attached

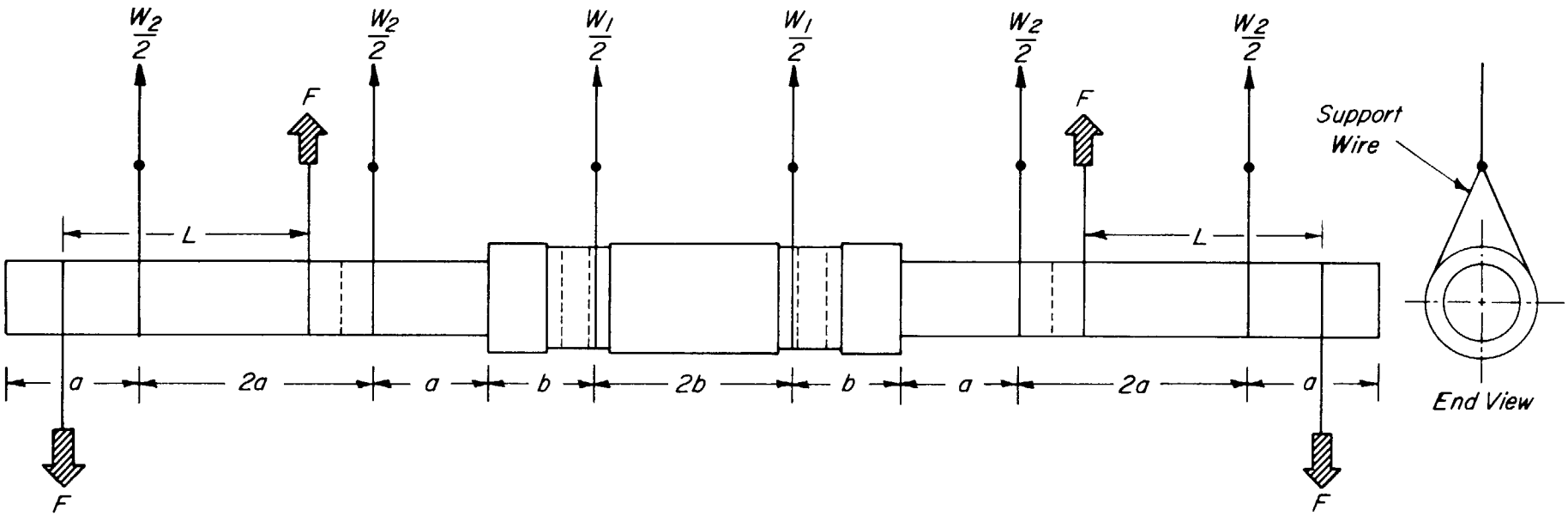

W_1 = Weight of Center Section plus Collars
W_2 = Weight of Stub Shaft plus Extensions
F x L = Input Moment

Scales:

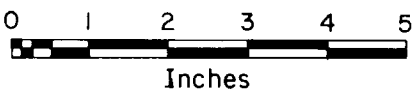

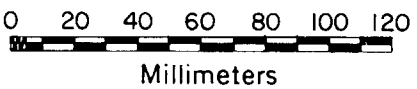

Figure 5 Schematic Diagram of Shaft Support Scheme

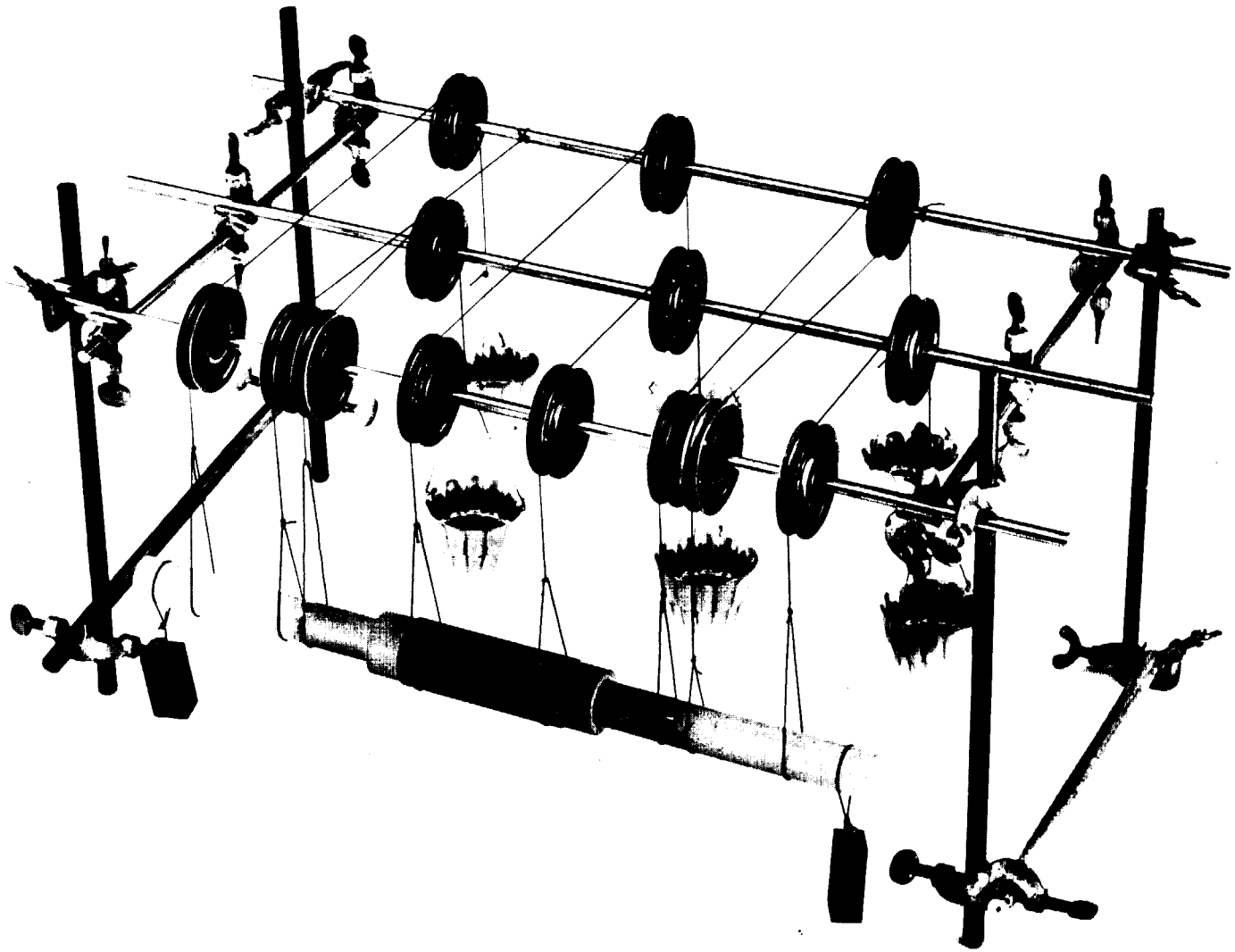

Figure 6 Counterbalance Jig Before Stress Freeze

Young's modulus was obtained by stress freezing a strip of model material in compression and by measuring a gage length before and after the freeze. This was done with each batch of model material to minimize errors resulting from changes in Young's modulus.

After the profile measurement was completed, the shaft was cut up in the geometry shown in Fig. 7. The model slices were polished, oiled for optical clarity and photographed in polarized light. Fig. 8 shows the centerline section fringe patterns.

7. Comparison of Theory and Experiment

The theoretical and converted experimental data appear in Fig. 2, which shows good agreement throughout most of the length of the shaft. The largest discrepancies are seen to occur near the center where the deflections would be of the order of the measurement precision. The most significant results are the indication of absence of stiffening from the collars, and the demonstration that elementary beam theory is adequate for predicting shaft deflections.

The small effect of the collars is understandable from the photoelastic fringe patterns in Fig. 8 which reveal the low fringe orders in the seats indicative of too small a pressure to aid the shaft. Also apparent are the stress concentrations at the section changes, which point up a new problem area now being investigated.

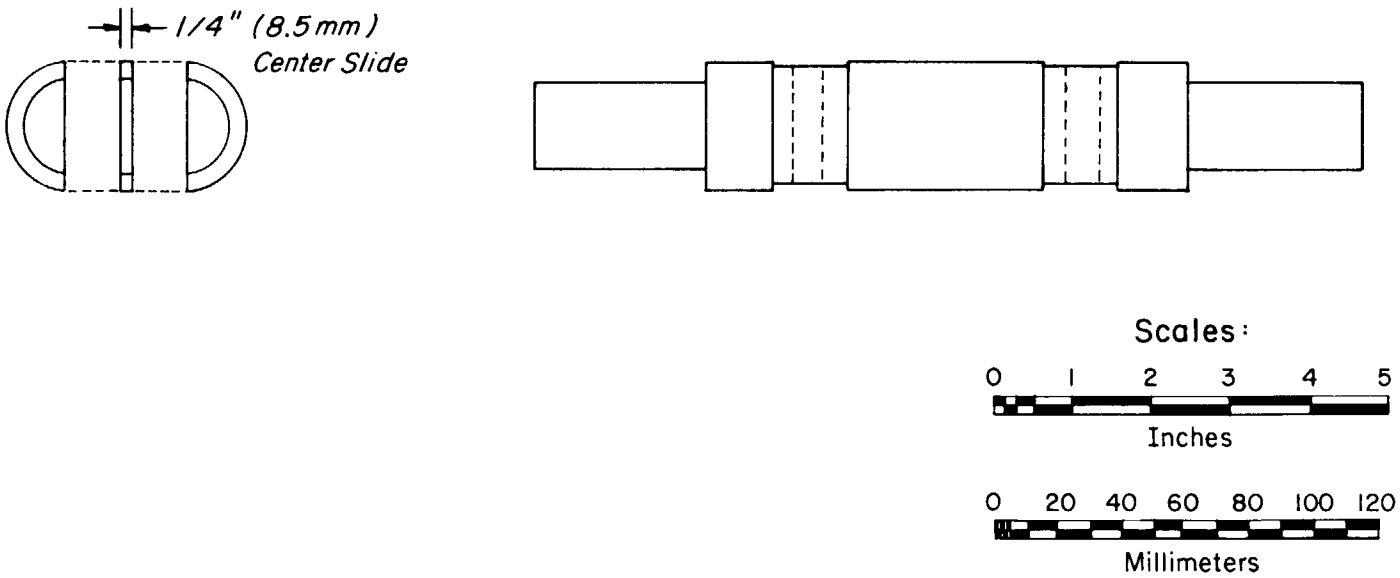

Figure 7 Methods of Photoelastic Sample Preparation

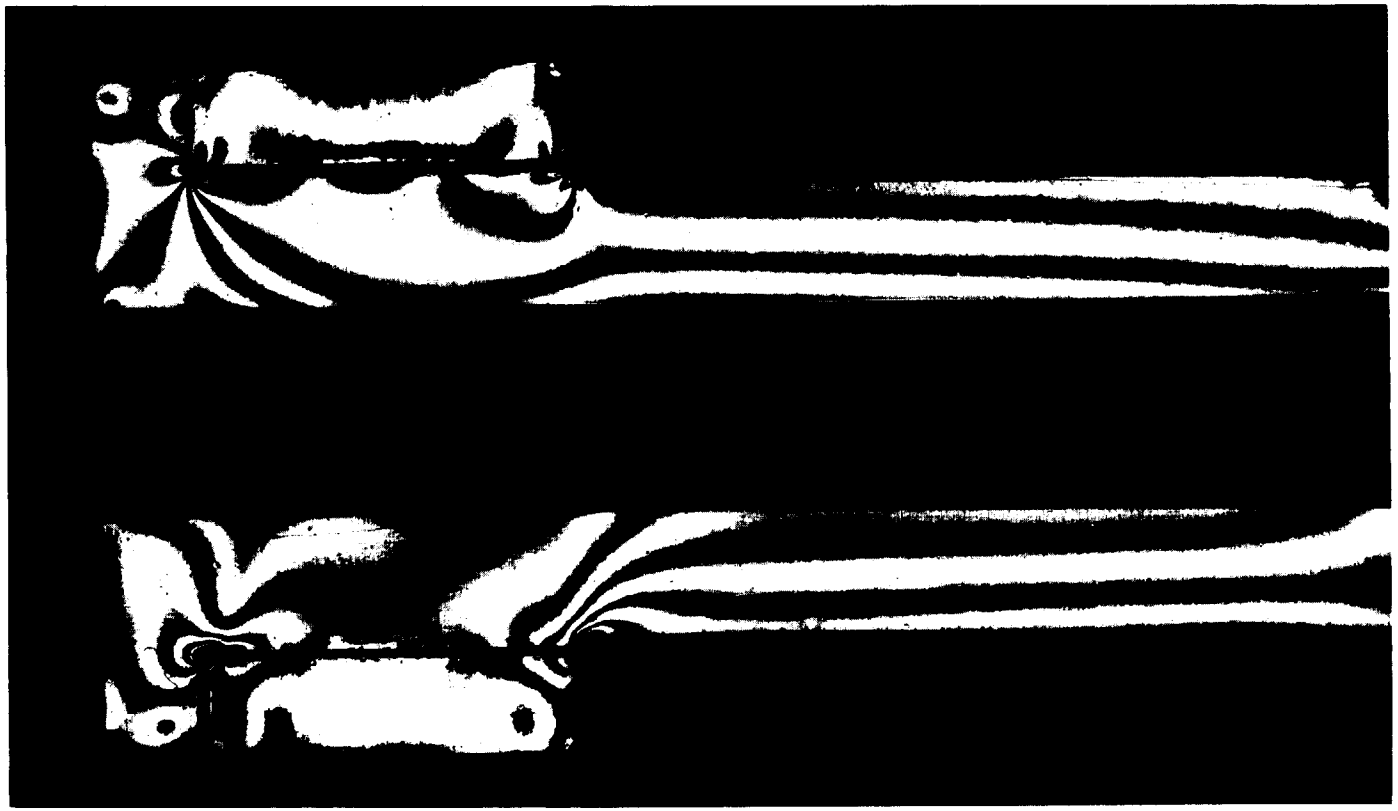

Figure 8 Fringe Pattern in Shaft With Bearing Collars. Bending Moment Only

INITIAL STUDY OF FORK OPTIMIZATION

A. Introduction

Optimization of the fork geometry in this initial phase required reaching a compromise between the short term strength of a quasistatic 100g handling shock load and the long term creep resistance to the stiffness dependent thermal stresses developed by 90 F (50 K) maximum temperature difference between the shaft and the cover. These could be contrary requirements. However, the fork would behave essentially as a pair of beams cantilevered from the cover plate. As a result, flexibility and strength are achievable with relatively wide, thin rectangular sections.

The shock loading is related to the short term yield strength of the fork material with stress concentrations playing an important role. The thermoelastic stresses should be kept below the level of the precision elastic limit (PEL) over a region of the fork and consequently stress concentrations may not be important. In this initial effort the current fork was found to be overly strong for shock and too rigid for the temperature condition of a hot shaft and a cold cover.

This initial optimization process involved analysis of stresses due to impact and temperatures. Utilizing these results together with PEL and yield strength information, the width and thickness of a constant section fork arm was determined.

B. 100g Normal to Shaft

The model for computing the stresses in the fork due to a load F acting at the center of the shaft in the direction normal to it is shown in Fig. 9. The internal forces S and M at the center are to be determined. Once this is done, the stresses in the shaft can be computed. The shear force S is determined from the condition of symmetry. Thus $S = F/2$. The moment M is determined from the continuity equation, i. e. ,

$$M\delta_m = S\delta_s$$

where δ_s and δ_m as depicted in Fig. 10, represent respectively the movements at the center of the shaft produced by unit shear and unit moment.

$$\delta_s = \delta_{1S} + \theta_{1S}\,\ell_1 + \delta_{2S} + (1/2)Lh(\theta/T)_f \tag{6}$$

$$\delta_m = \delta_{1m} + \theta_{1m}\ell_1 + \delta_{2m} + h(\theta/T)_f \tag{7}$$

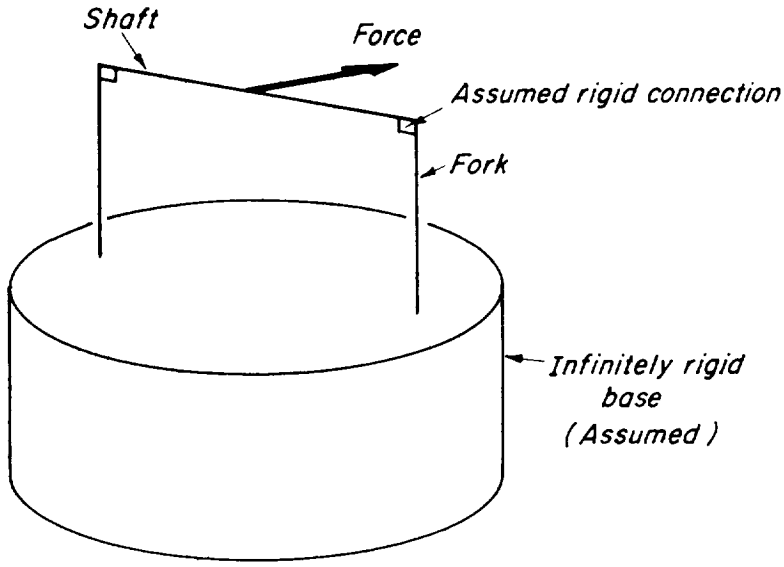

Figure 9 Schematic of Structure for 100g Transverse to Shaft

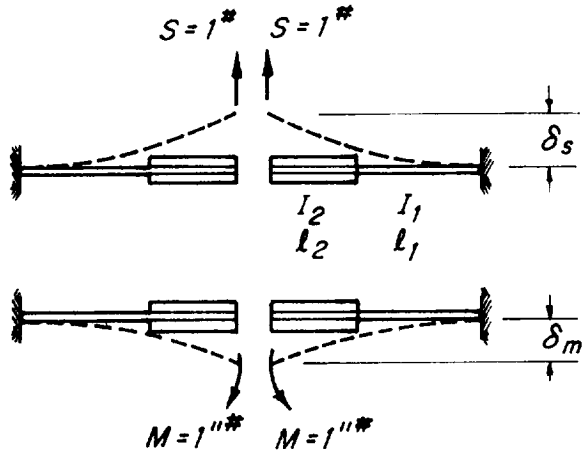

Figure 10 Internal Forces and Deflections on Shaft for Transverse 100g

3447

where $\delta_{1s} = \ell_2 \ell_1^2/2EI_1 + \ell_1^3/3EI_1$

$\theta_{1s} = \ell_2 \ell_1/EI_1 + \ell_1^2/2EI_1$

$\delta_{2s} = \ell_2^3/3EI_2$

$\delta_{1m} = \ell_1^2/2EI_1$

$\theta_{1m} = \ell_1/EI_1$

$\delta_{2m} = \ell_2^2/2EI_2$

$(\theta/T)_f$ = angle of twist of fork per unit length per unit torque as determined from Ref. (1)

L = Length of shaft

h = Height of fork

After M is known, the torque T on the fork can be determined as

$$T = M - S(L/2)$$

The applied load F at the center of the shaft is 100 mg = 100 W, where W is the weight of the assemblage of the rotor, stator and shaft. Using this load and the dimensions of the fork given in Ref. (1), the bending moment and stresses in the fork were computed as in Fig. 11. The maximum shear stress in the fork was computed as 1260 psi (8.7 n/mm^2) from Eq. (5.46) in Ref. 3.

C. 100g Parallel to Shaft

The model for computing the stresses in the fork due to a load F acting at the center of the shaft in the direction parallel to it is shown in Fig. 12. The internal forces P and S at the center are to be determined. Once this is done, the stresses in the fork can be computed, for they are caused by P and S. The axial force P is determined from the condition of asymmetry, P = F/2. The shear force S is determined from the continuity equation, i. e. ,

$$S\delta_s = P\delta_p$$

where δ_p and δ_s, as depicted in Fig. 13, represent respectively the movements at the center of the shaft produced by unit axial force and unit shear.

$$\delta_p = L(\theta/p)_f$$

$$\delta_s = \left[(\theta/m)_f + (\theta/m)_c \right] L^2/2 + 2(\delta/S)_{sh}$$

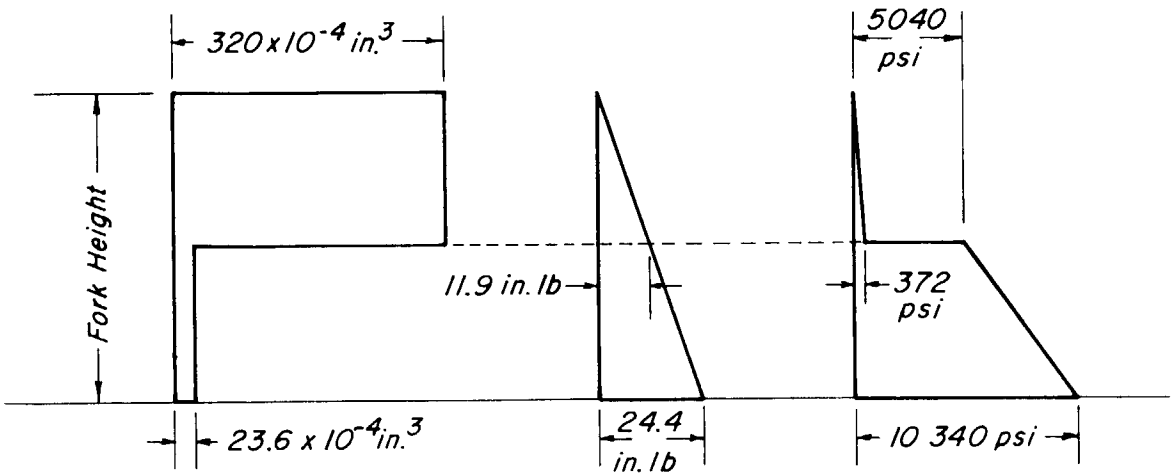

Conversions:

1 in. = 25.4 mm

1 in. lb = 113 mm n

1 psi = 6.89 x 10^{-3} n/mm^2

Figure 11 Bending Stresses in Fork Under Transverse 100g

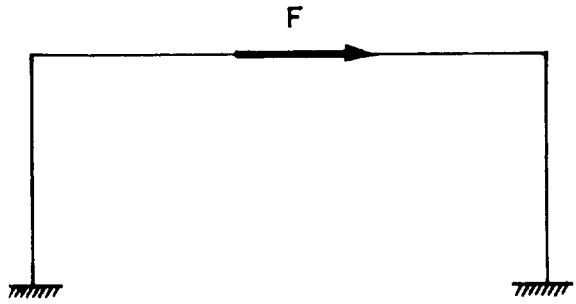

Figure 12 Schematic of Structure for 100g arallel to Shaft

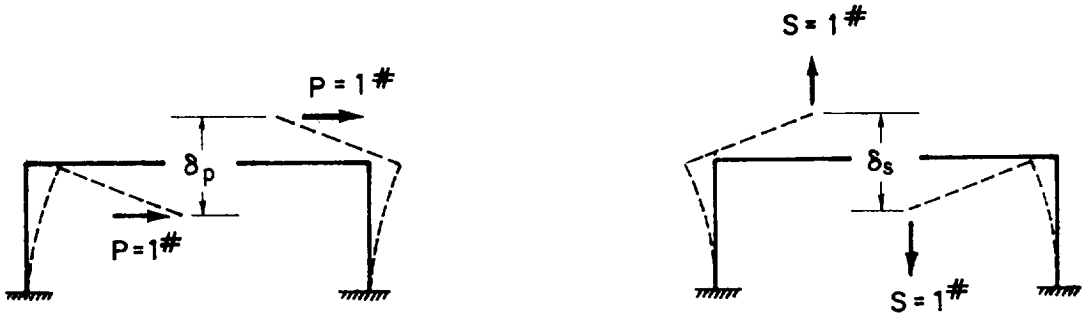

Figure 13 Internal Forces and Deflections for 100g Parallel to Shaft

5452

Here $(\theta/p)_f$ = rotation of the upper end of fork caused by a unit shear

$(\theta/m)_f$ = rotation of the upper end of fork caused by a unit end moment

$(\theta/m)_c$ = rotation of the clamp caused by a unit moment

$(\delta/S)_{sh}$ = displacement at the center of the shaft caused by a unit shear at the center

$$= \delta_{1S} + \theta_{1S}\,\ell_1 + \delta_{2S}$$

The values of $(\theta/p)_f$, $(\theta/m)_f$ and $(\theta/m)_c$ were assumed to be equal to those given in Ref. 1. Then the moment at the upper end of the fork caused by the shear force S is given as

$$M = (1/2)SL$$

The applied load F at the center of the shaft, in the direction parallel to it, is 100W. Using this load and the dimensions of the fork given in Ref. 1, the bending moment and maximum fiber stresses in the fork were computed as in Fig. 14.

D. Impact Test - Shaft and Fork

The quasistatic analysis of the 100g impact assumes essentially cantilever bending of the fork at the fundamental frequency. In order to obtain an estimate of the validity of this concept, a simple test was conducted with the apparatus shown in Fig. 15 to produce impact parallel to the shaft. The fringe patterns were recorded with a Fastax camera at 5900 frames/sec. The sequence of frames is shown in Fig. 16 which clearly reveals a nearly pure cantilever bending fringe pattern in the polariscope embedded in one fork arm (Fig. 17). This simple result would tend to support the quasistatic impact analysis.

E. Assumed 90F (50K) Shaft/Fork Temperature Differential

The model for computing the stresses in the fork due to an extreme temperature difference of 90 F (50 K) between the fork and shaft was the same as the one used in Ref. 1. The internal moments M at the ends of the forks are given by Eq.(34) of the same reference. The internal axial force P in the shaft can be computed from the following equation:

$$P = \left[\frac{(\theta/M)_f + (\theta/M)_c + (\theta/M)_s}{(\theta/P)_f}\right] M$$

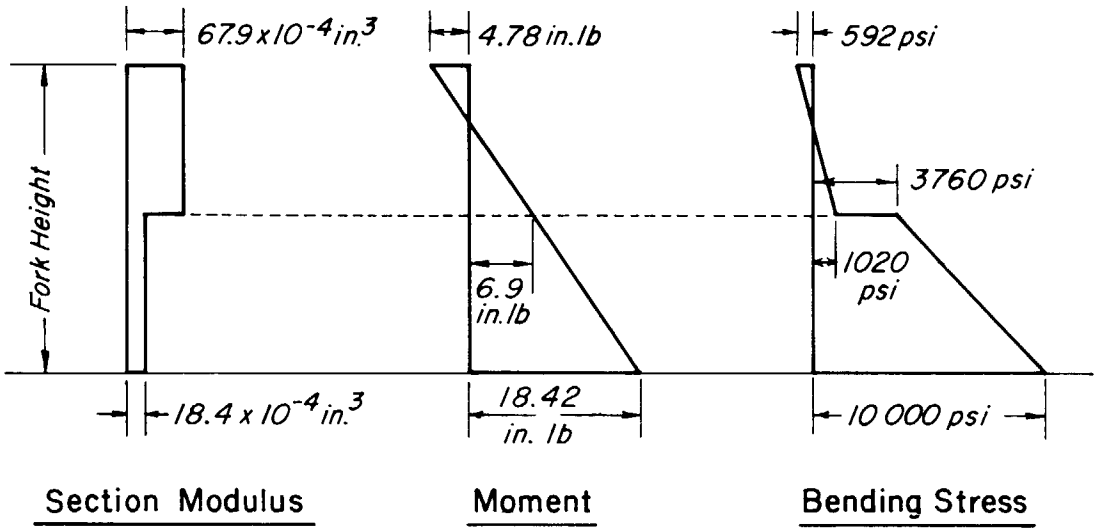

Conversions:

1 in. = 25.4 mm

1 in. lb = 113 mm n

1 psi = 6.89 x 10^{-3} n/mm^2

Figure 14 Stresses in Fork Under 100g Parallel to Shaft

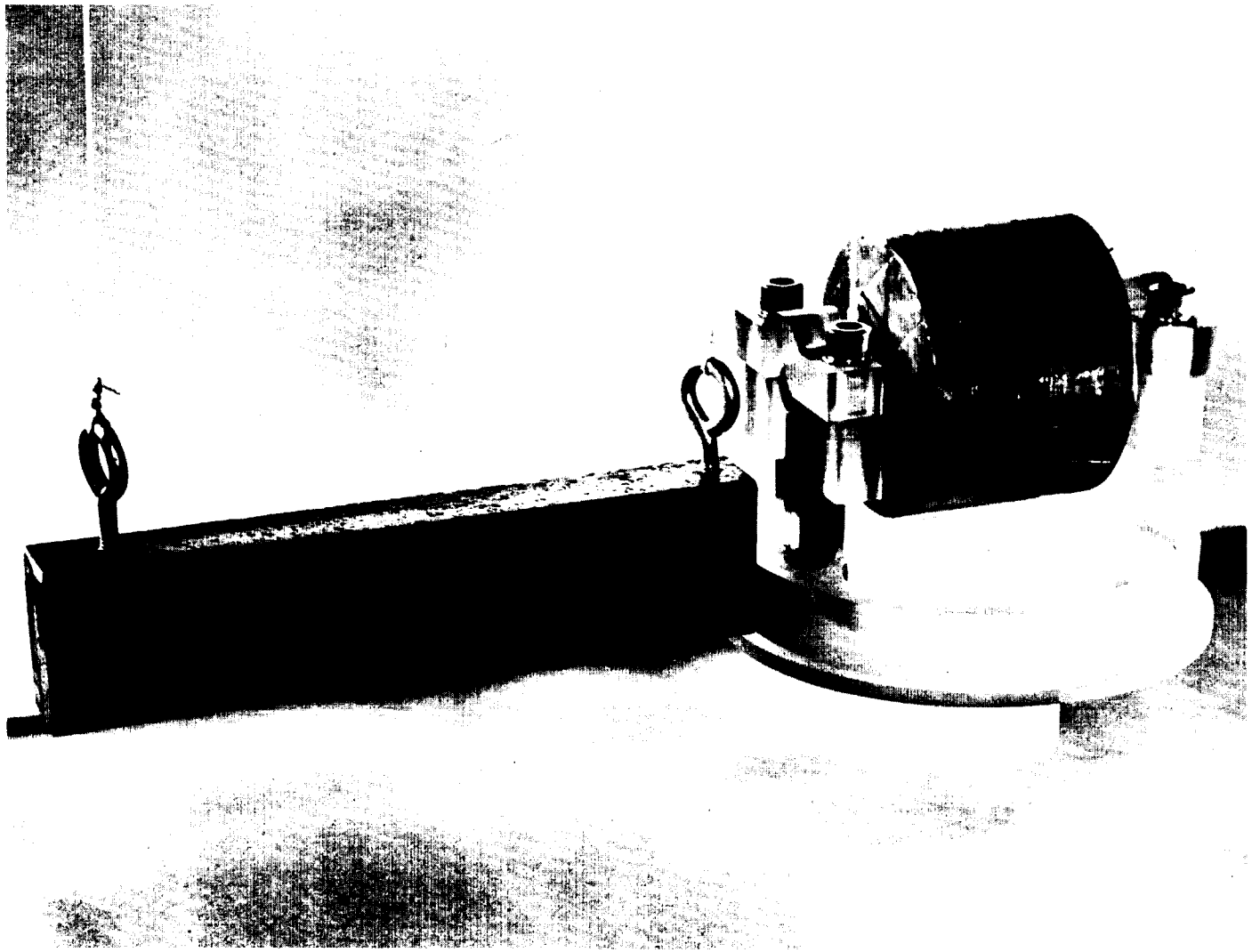

Figure 15 Impact Test Apparatus

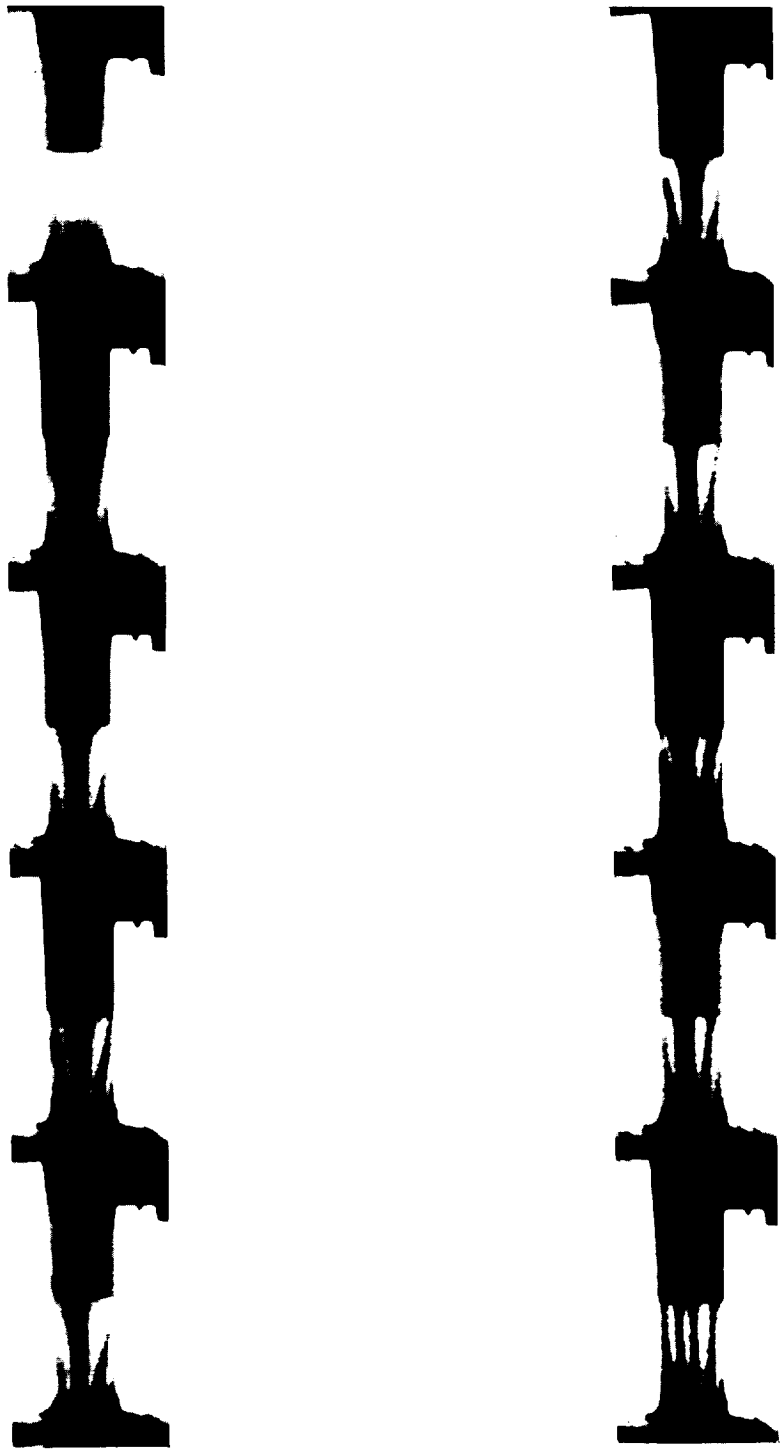

Figure 16 Photoelastic Fringe Patterns During Impact Loading on Fork Arm Model

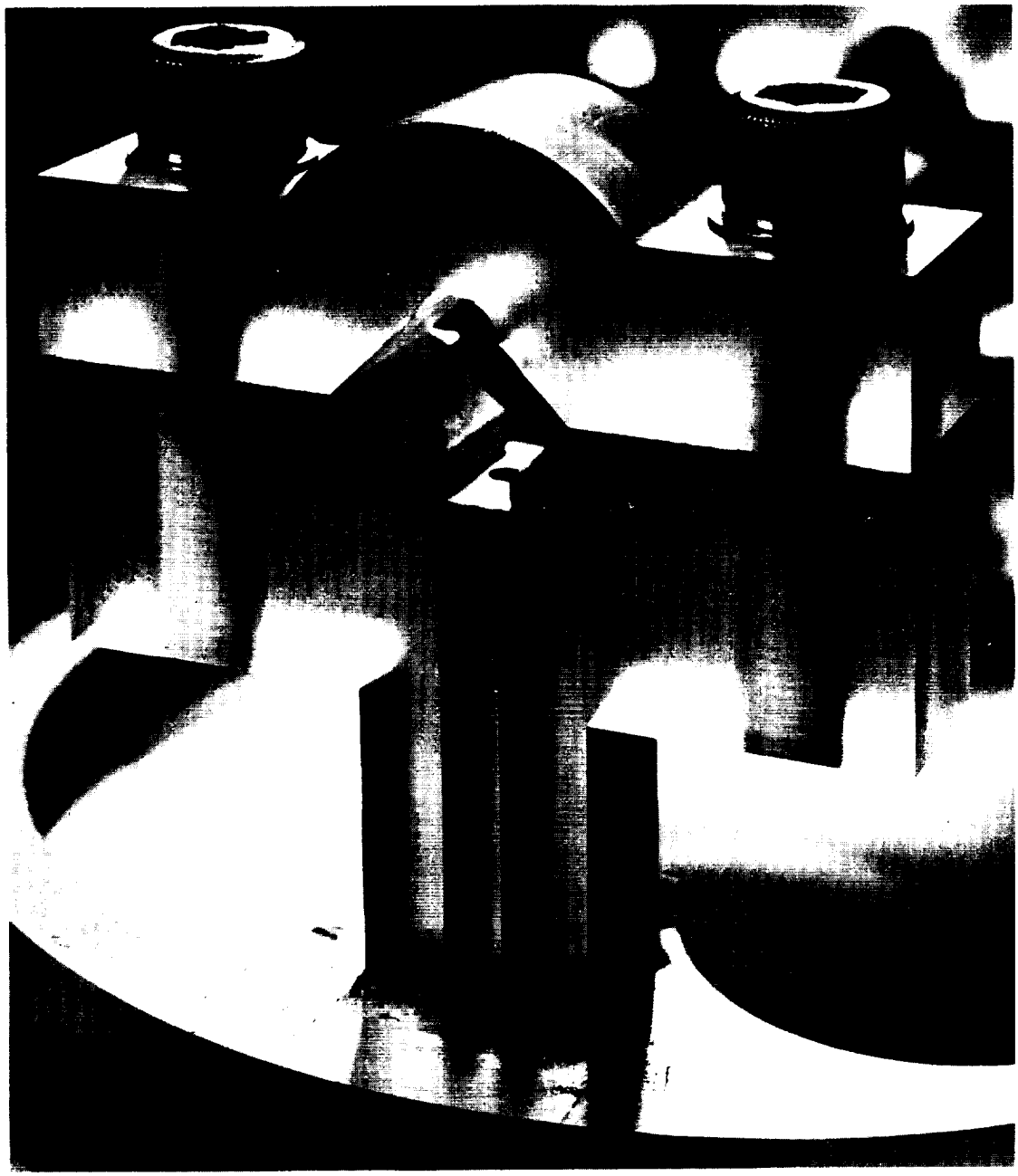

Figure 17 Fork Arm Model Showing Embedded Polariscope

which is derived from Eqs. (32) and (33) of Ref. 1 together with the consideration of the clamp flexibility. Here $(\theta/M)_f + (\theta/M)_c = 93.2\ (1 + 0.22)$; $(\theta/M)_s = 134.4$; and $(\theta/P)_f = 42.8$ as given in Ref. 1. Once P and M were determined, the stresses in the forks were computed. Fig. 18 shows the moments and maximum stresses in the fork due to the 90F (50K) temperature difference.

F. Fork Optimization

The preceding data on fork stresses, and the information to be discussed subsequently on beryllium yield strength and PEL, provide the background for optimizing the gyro fork. As indicated below, however, the PEL for S-100 is only about 2000 psi (13.8 n/mm^2) maximum. Consequently the temperature induced stress level of 7440 psi (51.3 n/mm^2) reported in Fig. 18 for the current fork would be too high, whereas the 10,000 psi (69 n/mm^2) stress for 100g shock would be safe even with a stress concentration factor of 3, since the 0.002 offset yield strength is reportedly 29,900 psi (206 n/mm^2). As a result the fork section rigidity for temperature stresses could be reduced without sacrificing impact strength.

For a rectangular cross section of width b and thickness h, the bending stress under a moment M would be

$$\sigma = 6M/bh^2 \tag{8}$$

In order to retain the impact strength, bh^2 could be maintained constant at the current $b_o h_o^2$ of 1.105×10^{-2} in^3 (180 mm^3), $b_o = 0.263$ in (6.7 mm), $h_o = 0.205$ in (5.2 mm). The bending stiffness of a fork arm would be proportional to bh^3, as was assumed for the force F under $\Delta T = 90$F (50K). For a new combination of b and h

$$F/F_o = bh^3/b_o h_o^3 \tag{9}$$

The stress at the fork root (where the moment due to ΔT would be greatest) would be (conservatively)

$$\sigma = 6FH/bh^2 = 2000 \text{ psi } (13.8 \text{ n/mm}^2) \text{ (S-100 PEL)} \tag{10}$$

Therefore

$$2000 = 6\ (F/F_o)F_o H/bh^2 = 6\ (bh^3/b_o h_o^3)F_o H/bh^2 \tag{11}$$

But at present

$$6F_o H/b_o h_o^2 = \sigma_o = 7440 \text{ psi } (51.3 \text{ n/mm}^2)$$

Therefore

$$2000 = (bh^3/b_o h_o^3)(7440)(b_o h_o^2/bh^2)$$

or

$$h/h_o = 2000/7440 = 0.27$$

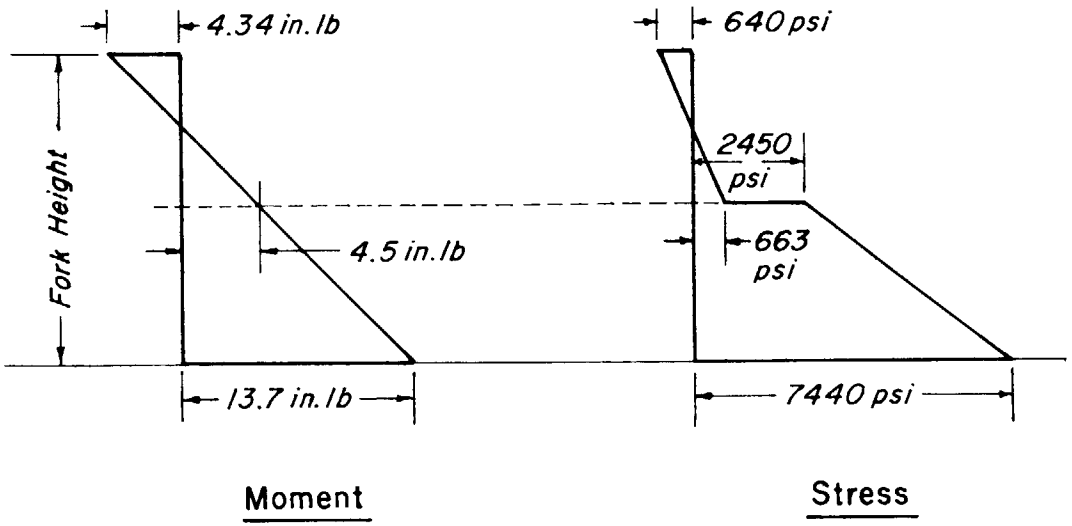

Conversions:

1 in. lb = 113 mm n

1 psi = 6.89 x 10^{-3} n/mm^2

Figure 18 Stresses in Fork Under 90F (50K) Temperature Differential

and consequently

$$h = 0.0554 \text{ in. } (1.4 \text{ mm}) \qquad (12)$$

$$b = 3.6 \text{ in. } (91.5 \text{ mm}) \text{ (since } bh^2 = 1.105 \times 10^{-2} \text{ in}^3 \text{ (180 mm}^3\text{)}$$

These cross section dimensions approximate an optimum fork of constant section. Calculations are now being made to refine this result for a fork cross section which varies with height H and which would be made of a beryllium with greater PEL. Also, more realistic temperatures and the finite rigidities of both the fork and shaft are being taken into account.

TRANSIENT THERMAL ANALYSIS

A. Introduction

A preliminary transient thermal analysis was conducted to obtain an understanding of the temperature behavior of the shaft in the region of the stator. The problem was simplified to a 2-component system consisting of the shaft and the stator, and an elementary computation was performed to obtain shaft temperature as a function of time.

One result was the indication that the simplified transient model yielded temperatures in fair agreement with previous steady state data reported in Ref. 1. Perhaps of more importance, however, was the prediction of an override of 46 F (26 K) in excess of the steady state temperature.

B. Method of Analysis

The analysis was conducted on the 2-element system depicted schematically in Fig. 19. The heat generation was confined to the stator, which was assumed to be attached to the shaft with perfect thermal contact. The shaft ends were assumed to be attached to beryllium extensions of a length representative of the distance to the bottom of the cover. Outside the region of the stator, the shaft area (and the beryllium extension also) were assumed constant. The far ends were considered to be held at 70 F (294 K). The basic equations used to solve the problem were the two expressions for transient heat flow:

In stator, $$Q - q_1 = (\rho c V)_1 (dT_1/dt) \quad (13)$$

In shaft, $$q_1 - 2q_2 = (\rho c V)_2 (dT_2/dt) \quad (14)$$

$$q_1 = k_1 A_1 (T_1 - T_2)/L_1 \quad (15)$$

$$q_2 = k_2 A_2 (T_2 - T_o)/L_2 \quad (16)$$

Then $$Q - k_1 A_1 (T_1 - T_2)/L_1 = (\rho c V)_2 (dT_2/dt) \quad (17)$$

$$k_1 A_1 (T_1 - T_2)/L_1 - 2k_2 A_2 (T_2 - T_o)/L_2 = (\rho c V)_2 (dT_2/dt) \quad (18)$$

The numerical values of the constants appear in the following listing:

k_1 = 42.4 btu/hr/ft/ F (7.78 Joule/hr/mm/ K)

k_2 = 96.7 btu/hr/ft/ F (17.76 Joule/hr/mm/K)

A_1 = 0.00924 sq. ft. (858.1 mm^2)

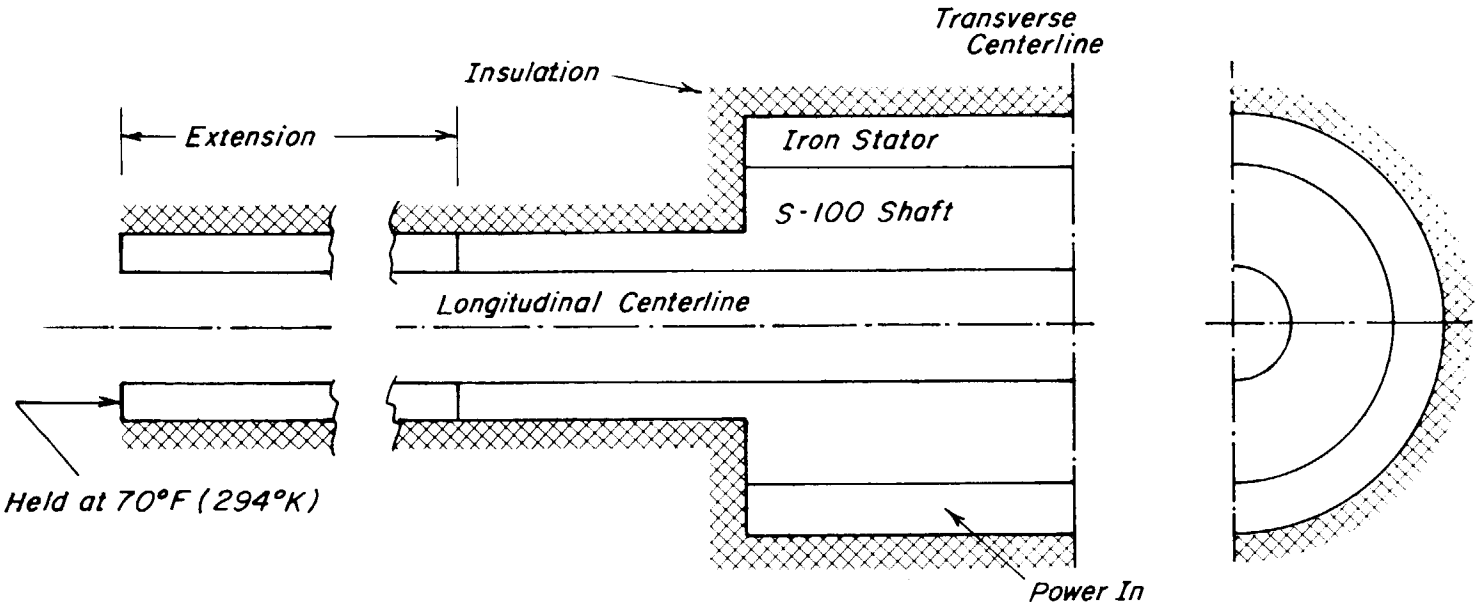

a. Basic Model

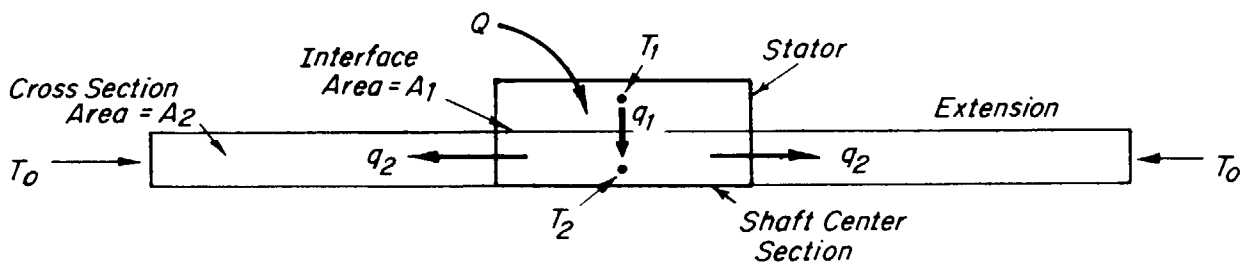

b. Mathematical Model

Figure 19 Schematic of Simplified Two Component Model for Transient Analysis of Shaft Temperatures

A_2 = 0.000156 sq. ft. (14.49 mm^2)

L_1 = 0.0283 ft. (8.625 mm)

L_2 = 0.0737 ft. (22.46 mm)

$(\rho cV)_1$ = 0.00485 btu/F (0.271 Joule/K)

$(\rho cV)_2$ = 0.00319 btu/F (0.1785 Joule/K)

Q = 61.5 btu/hr. (1910.2 Joule/hr) (for the first 90 seconds)

Q = 27.4 btu/hr. (851.04 Joule/hr) (after the first 90 seconds)

By differentiation of Eq. (18) employing the numerical constants and letting $T_o = 0$, the following second order differential equation in T_2 was obtained:

$$10^{-3}d^2T_2/dt^2 + 7.34\, dT_2/dt + 366T_2 = 55200 \quad \text{for } Q = 61.5 \text{ btu/hr} \tag{19a}$$

$$10^{-3}d^2T_2/dt^2 + 7.34\, dT_2/dt + 366T_2 = 24600 \quad \text{for } Q = 27.4 \text{ btu/hr} \tag{19b}$$

The solution was achieved by numerical computation using a variation of forward differences.

The stator temperature T_1 would be only a few degrees higher than the shaft center section, as can be observed from Eq. (17). Since Q is constant during startup for the first 90 seconds, then the largest possible difference between T_1 and T_2 would occur with the smallest dT_1/dt. If this quantity is arbitrarily chosen equal to zero, then

$$T_1 - T_2 = QL_1/k_1A_1 = 4.44 \tag{20}$$

Therefore, the stator temperature would be expected to exceed the shaft temperature by less than 4.44 F (2.45 K), according to the preceding simplified analysis.

C. Results

The power input which was assumed for the analysis is shown in Fig. 20, together with the temperature predicted in the central region of the shaft within the stator. The Ref. 1 steady state result for 70 F (294 K) gas bearing temperature and 8 watts input is shown at the right for comparison.

Peak temperature would be attained at the time of power reduction (1 to 1-1/2 minutes after start-up). This would be followed by an asymptotic decay from the override to the steady state condition after several more minutes.

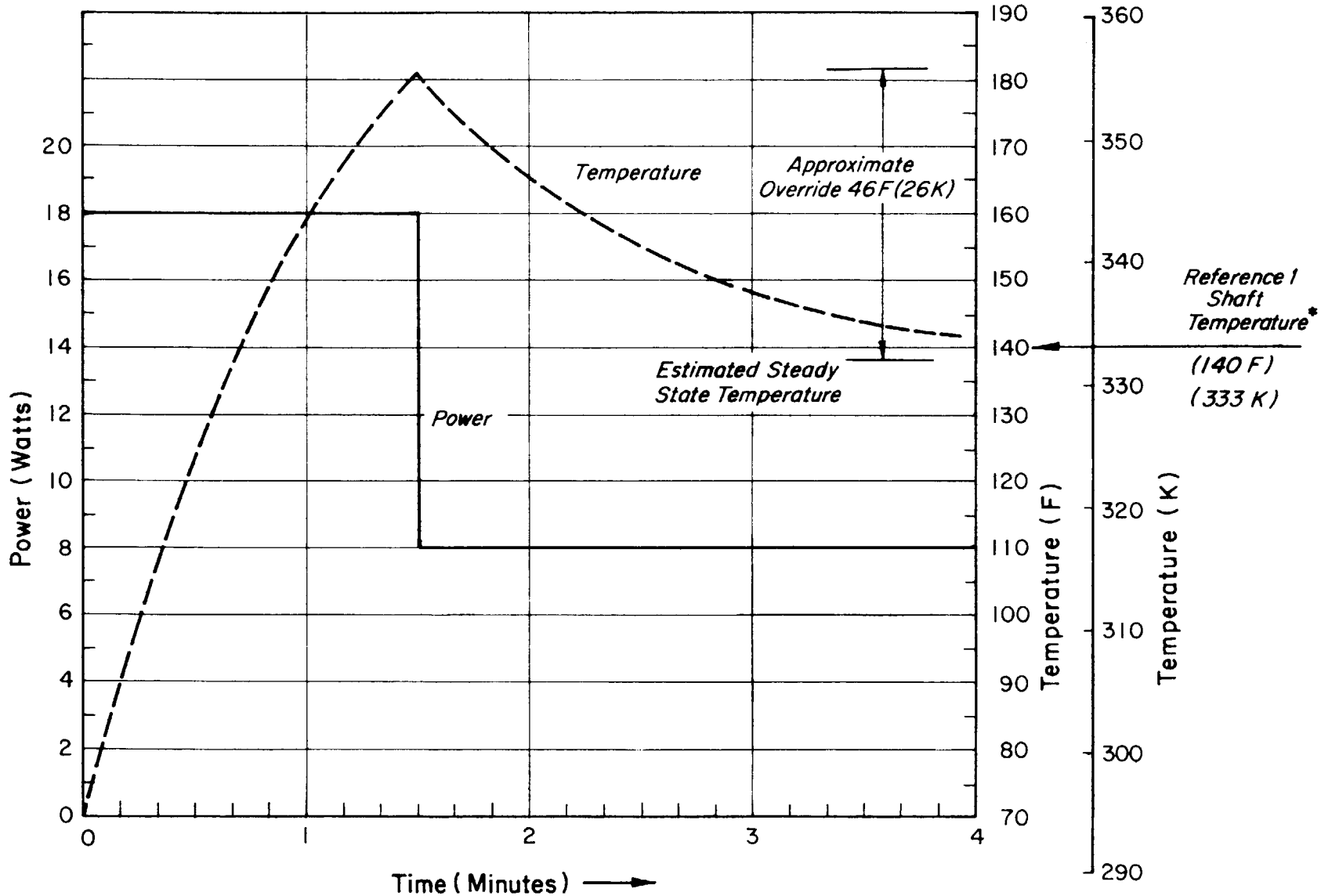

Figure 20 Specified Power Input and Predicted Temperature at Central Region of Shaft Within Stator

*Ref. 1 Shaft temperature for steady state motor temperature of 158F(343K) and gas bearing temperature 70F(294K) and 8 watts input

D. Optimum Startup

One possible method of avoiding the temperature override is through consideration of continuous power application employing Eq. (21) to select the power as a function of time. Therefore, the constants on the right side of Eq. (19) would be replaced by a function of time so that

$$d^2T/dt^2 + a\, dT/dt + bT = Af(t) \tag{21}$$

where A converts the power f(t) into the proper units for Eq. (21).

A commonly used function for an asymptotic temperature transient is

$$T = T_o(1 - e^{-st}) \tag{22}$$

If this result is substituted into Eq. (21), it is found that the corresponding power input should have the form

$$f(t) = (T_o/A)[b - e^{-st}(k^2 - ak + b)] \tag{23}$$

This is only one of a number of possibilities. If a different type of power input is desired for performance control, Eq. (21) still could yield a good first approximation to determination of the numerical values of power to maintain the shaft temperature during startup at a level no greater than during steady state.

MICROPLASTICITY

A. Introduction

The AB5-K8 gyro has structural members fabricated of beryllium. As part of this structural investigation the low stress level behavior of beryllium was examined in an attempt to determine microplastic response. Since internal displacements of the order of one microinch may have an effect on instrument precision and accuracy, it was appropriate to study stress behavior which would result in permanent strains of the order of 10^{-5} to 10^{-7}.

A quantity of beryllium, Bendix material specification ECL-450 Grade A, was obtained. (This is similar to Brush S-100.) Bending tests were performed to obtain the precision elastic limit (PEL) and a limited amount of microcreep data. In the course of these experiments, data were also obtained on the Micro-Bauschinger effect using reverse loading in the bending experiments. Two types of specimens were employed, one flat and the second an I-beam. The flat specimen was loaded into the microplastic region for subsequent examination by electron microscope for etch pits. The majority of the microstrain data were obtained from the I-beam specimen.

This section describes the experiments completed to date and presents the significant analyzed test data. As a result of the tests, conclusions regarding the possible behavior of this material in a structure are presented and are compared with data on other materials. Additional tests of other materials are in progress and the test results will be reported at a later date, together with the results of the electron microscopy studies.

B. Experimental Procedure

1. Material

Five round bars of beryllium, Bendix Material Specification ECL-450, Issue A, Grade A, 0.375 in. (9.52 mm) diameter and 12 in. (305 mm) long were obtained from Brush Beryllium Corp., designated by Brush as QMV Beryllium Rod. This material has been reported to correspond to material used by the Astrionics Laboratory in the fabrication of the AB5 gyro. Chemical and processing data for the specimen material are given in the appendix. It should be noted that the "Grade A" in the specification refers to a material of high purity with minimum beryllium oxide content.

2. Experiment Design

Microplasticity experiments, which are summarized in Ref. 4, have been performed using both uniaxially loaded specimens and bending specimens, and each type of test has found its protagonists. There is no clear cut advantage of one type over the other and each has its disadvantages. The two major difficulties in microstrain experiments involve the operation of strain measuring equipment of suitable sensitivity and the ability to eliminate spurious strains due to thermal expansion. Using high sensitivity capacitance strain gages on uniaxial specimens, research workers have been able to measure in the 10^{-7} to 10^{-8} strain range; however, elaborate temperature control and compensation techniques have been required (see Ref. 4 for example). One can appreciate the difficulties in temperature control by noting that a strain change of 10^{-7} in beryllium can result from a temperature change of only 0.016 F (0.0088K).

Other experiments have been performed in the 10^{-5} to 10^{-7} strain range with strain gages on flat bending specimens using the four point loading scheme (Ref. 4). Inherent advantages of this system are the ease with which thermal strains can be compensated and the ease with which measurements can be made. There are some difficulties due to the stress gradient in the specimen and uncertainties as the surface stress value using the four point bending jig.

It appeared possible to minimize the instrumental and temperature control problems associated with the uniaxial specimens by using an improved bending arrangement. As a first step the common four point bending jig was abandoned in favor of an analagous whiffletree configuration which photoelastic tests had shown to apply a calculable bending moment to a specimen. The stress gradient effect was reduced in the specimen by using a modified I-beam configuration. A simple strip specimen was also tested. However, the strain gage data were used for comparison purposes only. The major objective in loading this specimen was to obtain a microstrained surface for examination with the electron microscope.

3. Specimen Configuration

The general I-beam specimen configuration is shown in Fig. 21. The restraining effect of the interior of the beam was reduced by using a thin web with large circular cut-outs. Sufficient material was retained in the web, however, to maintain the flexure curvature of the flanges under load, thereby permitting the use of the simple beam formula to compute the outer fiber stresses.

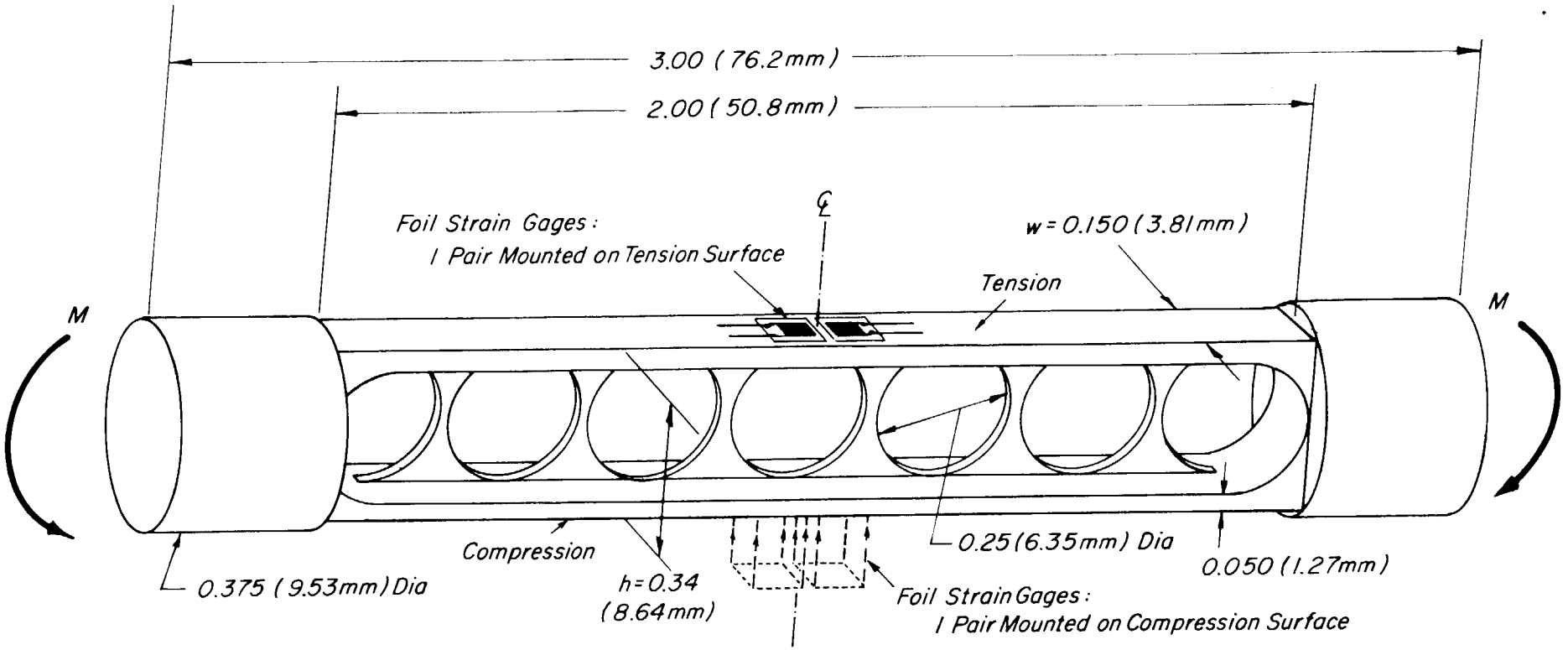

Figure 21 I-Beam Bending Test Specimen Dimensions

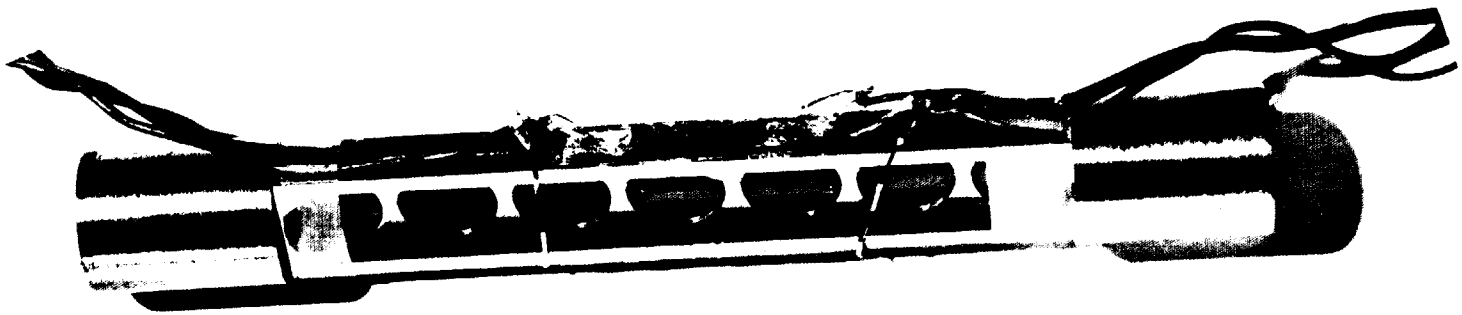

Figure 22 I-Beam Specimen With Strain Gages Installed

Two specimens were machined from nominal 3/8 in. (9.5 mm) diameter bar. After machining, a stress relief treatment consisting of the following was performed:

(1) vapor degrease,

(2) heat in vacuum (1 micron) to 1325 F (992K) and hold 1 hour,

(3) furnace cool to room temperature.

Two strip specimens 0.062 x 0.375 x 2.00 in. (1.59 x 9.52 x 50.8 mm) were also machined from the same bar stock and stress relieved. One of these was to be strained and then its surface, after proper treatment, compared with that of the remaining unstrained strip using electron microscopy.

4. Strain Gage Instrumentation

Pairs of foil strain gages BLH Type FAP-12-12S6, with a nominal 1/8 inch (6.45 mm) gage length were installed on each surface of the specimen using SR-4 cement. The gages were connected in a full bridge arrangement and the strains were read using a BLH Model 120A strain indicator. From the full bridge arrangement several major advantages accrue:

(1) The specimen outer fiber strain value is multiplied four times in the readout instrument. Since with the Model 120A, 10^{-6} can easily be read, strains of the order of 0.25×10^{-6} can be measured.

(2) All four bridge elements are identical and all are mounted on the specimen. Hence, the system is temperature self compensating. Only temperature gradients in the specimen which change with time can lead to erroneous strain readings.

Long time tests on unloaded specimens confirmed the anticipated stable behavior of this arrangement.

A photograph of an instrumented I-beam specimen is shown in Fig. 22.

5. Loading System

A simple whiffletree arrangement was installed in an ARA precision pneumatic testing machine shown in Fig. 23. A pure bending moment was introduced into the specimen by means of a lever arrangement with a one-inch moment arm shown in Fig. 24. Loads were controlled using the testing machine control console. However, since the anticipated loads were quite small with a 25 lb. (111 newton) maximum, a calibrated Hunter spring dynamometer was used as a load indicator rather than the testing machine load indicator.

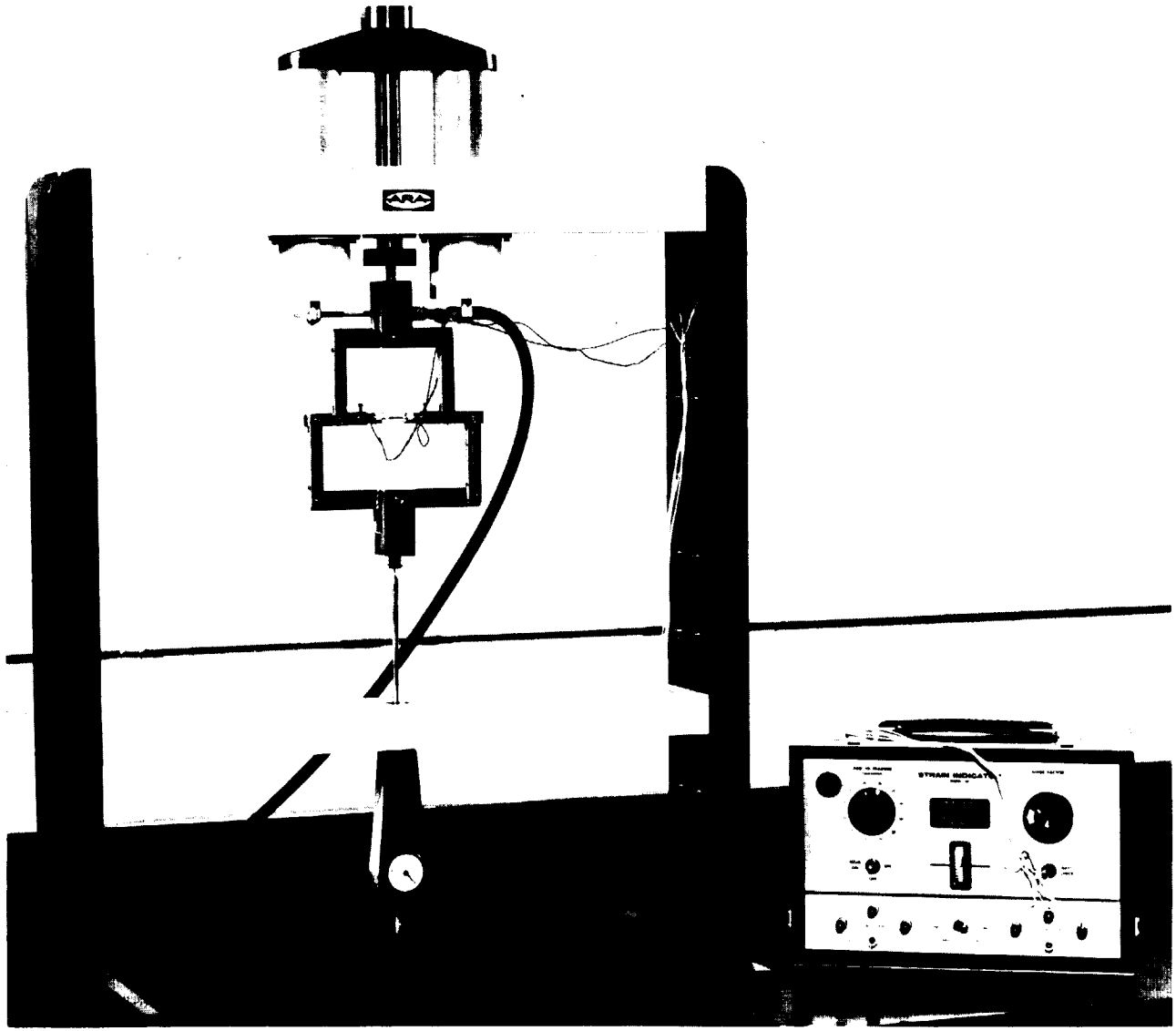

Figure 23 Bending Test Apparatus

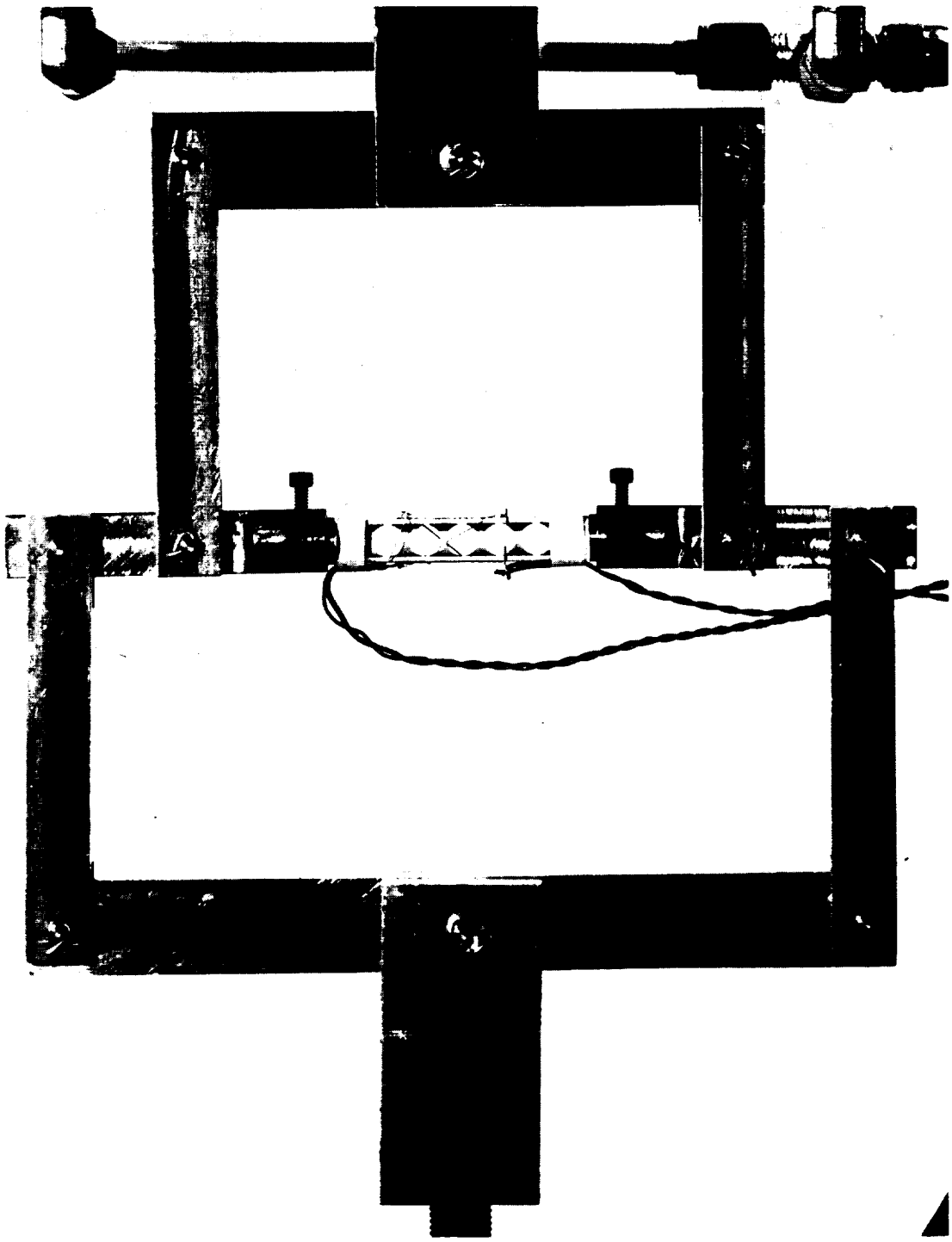

Figure 24 Loading Whiffletree with I-Beam Specimen Installed

6. Test Procedure

As a first step in the procedure, the strain indicator was turned on and the gages were allowed to stabilize. Tests showed that a gage with fully cured cement would stabilize in a few minutes. The change in strain reading during this period was ordinarily less than 0.5×10^{-6}. After stabilization, the first load increment was applied, the strain was recorded, the specimen was unloaded and the strain was measured again. The procedure was repeated each time with increasingly larger load increments. Care was taken to minimize creep in the specimen during this process by holding the maximum load in each increment only long enough for the strain indicator to be balanced - no more than a few seconds for each loading.

The flat electron microscope specimen was loaded up to a stress level of 12,000 psi (82.7 n/mm^2) in this fashion. No further incremental loading tests were performed since the strain readings showed that over 5×10^{-6} permanent plastic strain had been sustained. The specimen was loaded to the same stress level and allowed to creep for 1/2 hour and unloaded. The specimen was removed and is now being prepared for electron microscope surface observation.

The I-beam specimen was subjected to the load-unloaded incremental process to a stress level of approximately 7000 psi (48 n/mm^2). Then a standard stress-strain test to the same stress level was performed to determine the "elastic" stress-strain behavior. The specimen was then rotated 180° about the longitudinal axis in the whiffletree and was incrementally reloaded. In this second loading the original tension flange was now loaded in compression and vice versa. A second standard stress-strain test was performed. Next the specimen was rotated back to the original position and retested and then it was reversed once again. The load reversals were done to study the Micro-Bauschinger effect.

C. Test Results and Discussion

The data were analyzed in a number of different ways to delineate various aspects of the microstrain behavior of beryllium as follows:

(1) Specimen Comparison: Flat bending vs I-beam
(2) Stress-Strain Behavior
(3) Precision Elastic Limit
(4) Micro-Bauschinger Effect
(5) Microcreep
(6) Comparison with other existing data.

1. Specimen Comparison

The flat bending specimen is relatively simple to fabricate and has been used in a number of microplastic experiments. The disadvantage is the existence of a large strain gradient from the center outwards. In such a specimen after loading, if the outer fibers have sustained a small permanent plastic deformation, a small distance inward from the surface, the material may still be elastic. This elastic material then acts to constrain the surface material. The net effect of such constraint is that the measured surface residual strains are smaller than the value which would be measured in a uniaxial test to the same maximum stress. The results of tests on the two types of specimens shown in Fig. 25 indicate dramatically the lessened stiffening effect of the I-Beam. The stress level required to produce a given amount of microstrain in the flat specimen was some two to three times higher than that in the I-beam specimen. Quantitative results from the flat specimen must be considered unreliable.

2. Stress-Strain Behavior

The stress-strain curve obtained from the first incremental load-unload test in shown in Fig. 26. It should be noted that the stress was returned to zero after each point on the curve and hence the results may not be strictly comparable to data obtained under monotonically increasing stress. The residual plastic strain after the test was completed is shown to be approximately 8×10^{-6}. A second loading of the specimen, using the conventional monotonic increase of load to a stress level of approximately 5,000 psi (34.5 n/mm^2) with immediate unloading to zero stress, showed no residual plastic strain. These results indicated that the strain gages were operating satisfactorily and were not giving anomalous strain readings. Similar elastic loading checks were made periodically through the test series and in no case did the residual indicated strain exceed 0.25×10^{-6}.

3. Precision Elastic Limit

By definition the precision elastic limit is the stress level at which the permanent plastic strain is 10^{-6}. The values for the initial and subsequent loadings are given in Table 2. Also given in the table are the maximum stress levels beyond which there was a permanent plastic strain of 0.25×10^{-6}.

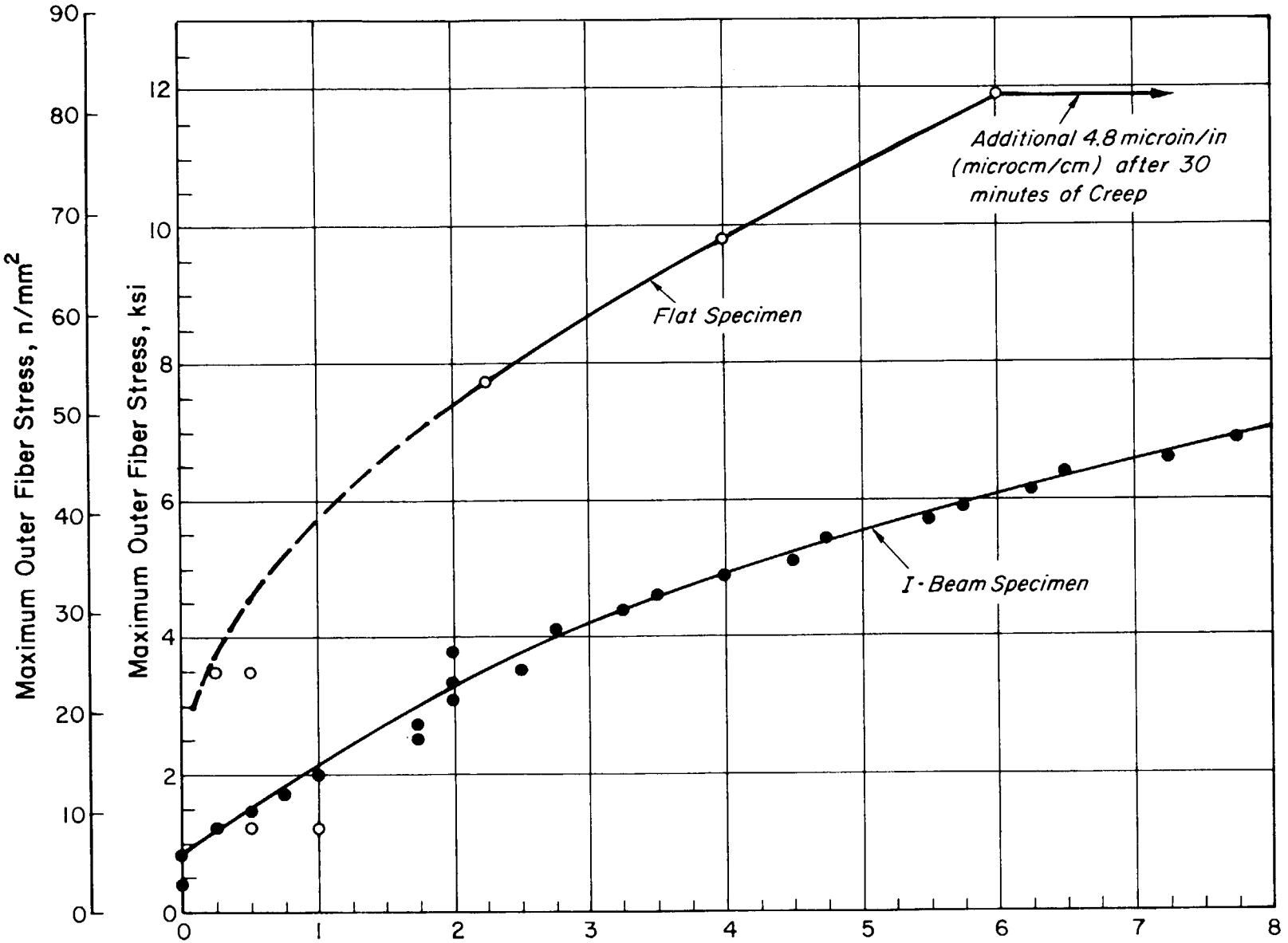

Figure 25 Residual Plastic Strain After Unloading in Flat and I-Beam Bending Specimens

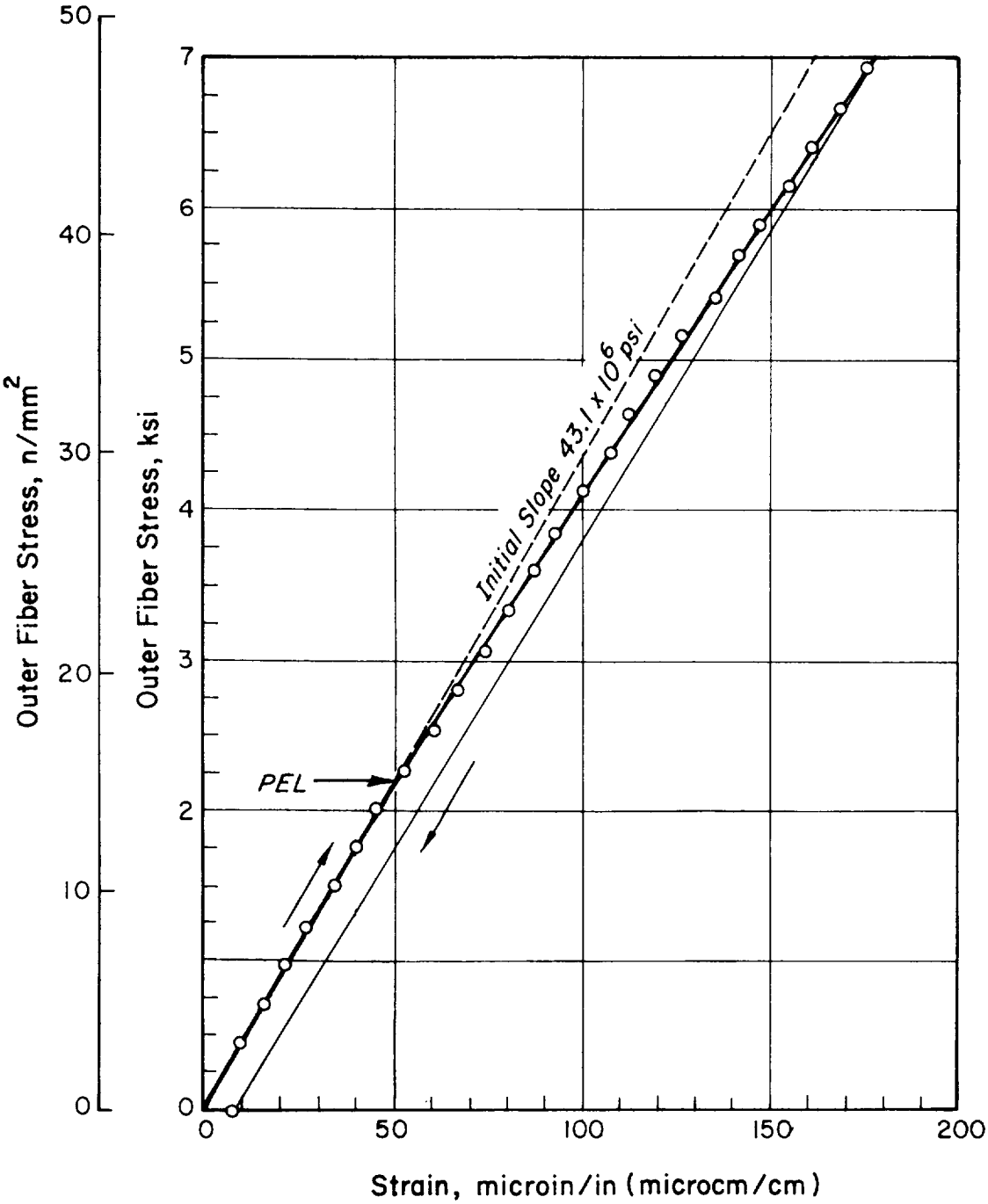

Figure 26 Stress-Strain Results from Load-Unload Test on I-Beam Specimen in Bending

5443

Table 2

	PEL (σ for $\epsilon_{pl} = 10^{-6}$)		(σ for $\epsilon_{pl} < 0.25 \times 10^{-6}$)	
Test*	psi	(n/mm^2)	psi	(n/mm^2)
Initial Loading	2010	(13.83)	961	(6.72)
First Reversal	1490	(10.25)	700	(4.82)
Second Reversal	1300	(8.94)	400	(2.75)
Third Reversal	1490	(10.25)	700	(4.82)

*Directions of initial loading and second reversal are the same and these are opposite to the directions of the first and third reversal.

4. Micro-Bauschinger Effect

The residual plastic strain data for four loadings, alternately changing direction, are shown in Fig. 27. In this figure the initial strain reading prior to the first loading was taken as zero strain and all other strains were referred to this same zero. A point on this diagram therefore represents the strain state after the specimen has undergone all the previous loading history. Using the same data as in Fig. 27, but treating each loading separately with the reference strain taken as the value at the beginning of each test, gives the results shown in Fig. 28. The observation that can be made here is that after a loading in one direction, the micro-plastic behavior in the opposite direction of loading was approximated by that of the original material and that after at least four of these loadings and reverse loadings no departure from this behavior was evident.

5. Microcreep

One microcreep test was performed on the flat strip specimen. After the last loading to a stress level of 11,900 psi (82 n/mm^2) and unloading, which produced a permanent strain of 6×10^{-6}, the specimen was returned to the same stress level and held for 1/2 hour. The additional permanent strain evident after unloading was 4.8×10^{-6}, indicating that room temperature creep can occur at low stress levels.

6. Comparison with Published Data

Published data on precision elastic limits of beryllium are contained principally in Refs. 5 - 8. These are summarized in Table 3.

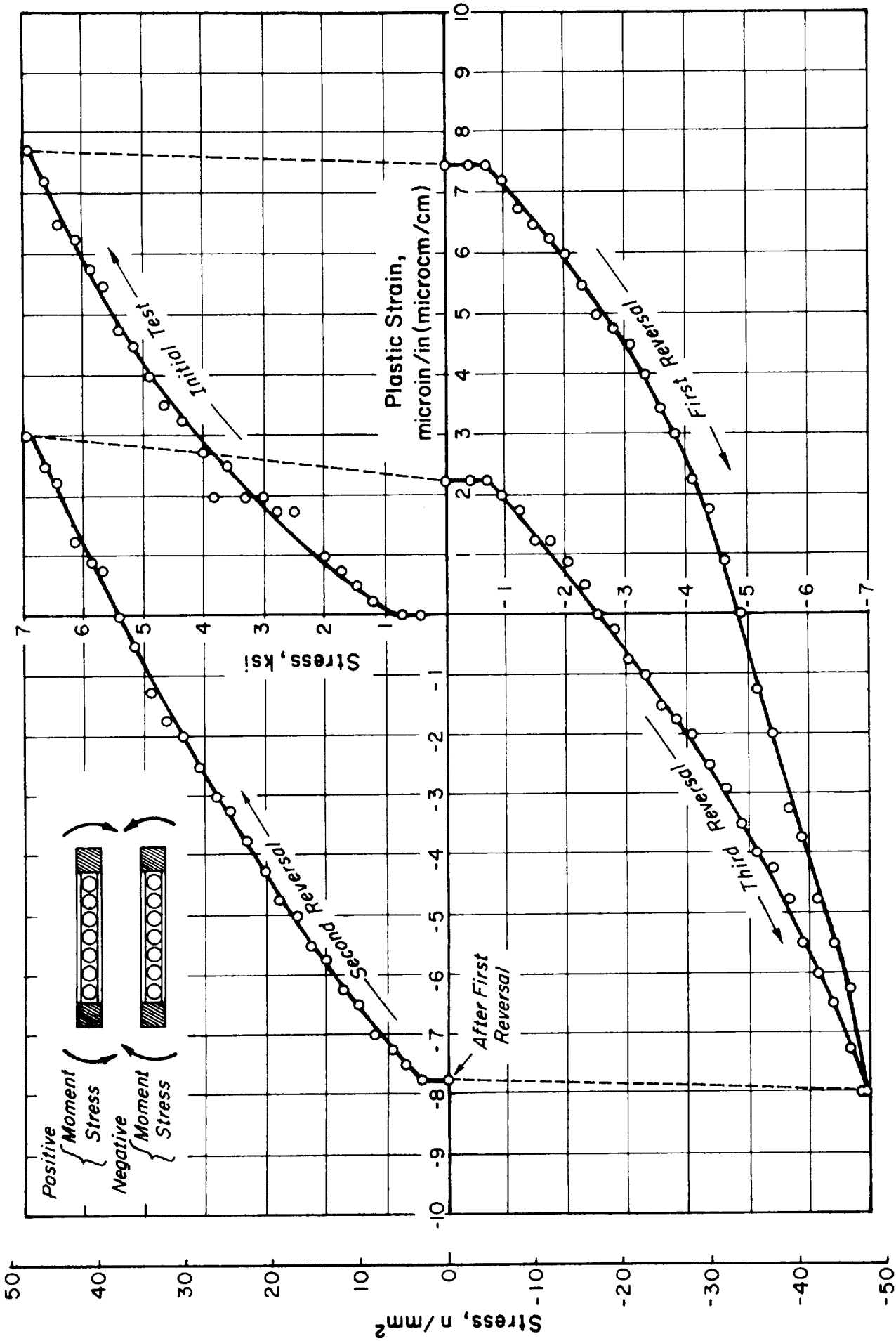

Figure 27 Residual Strain History for Four Loading Tests on I-Beam Specimen

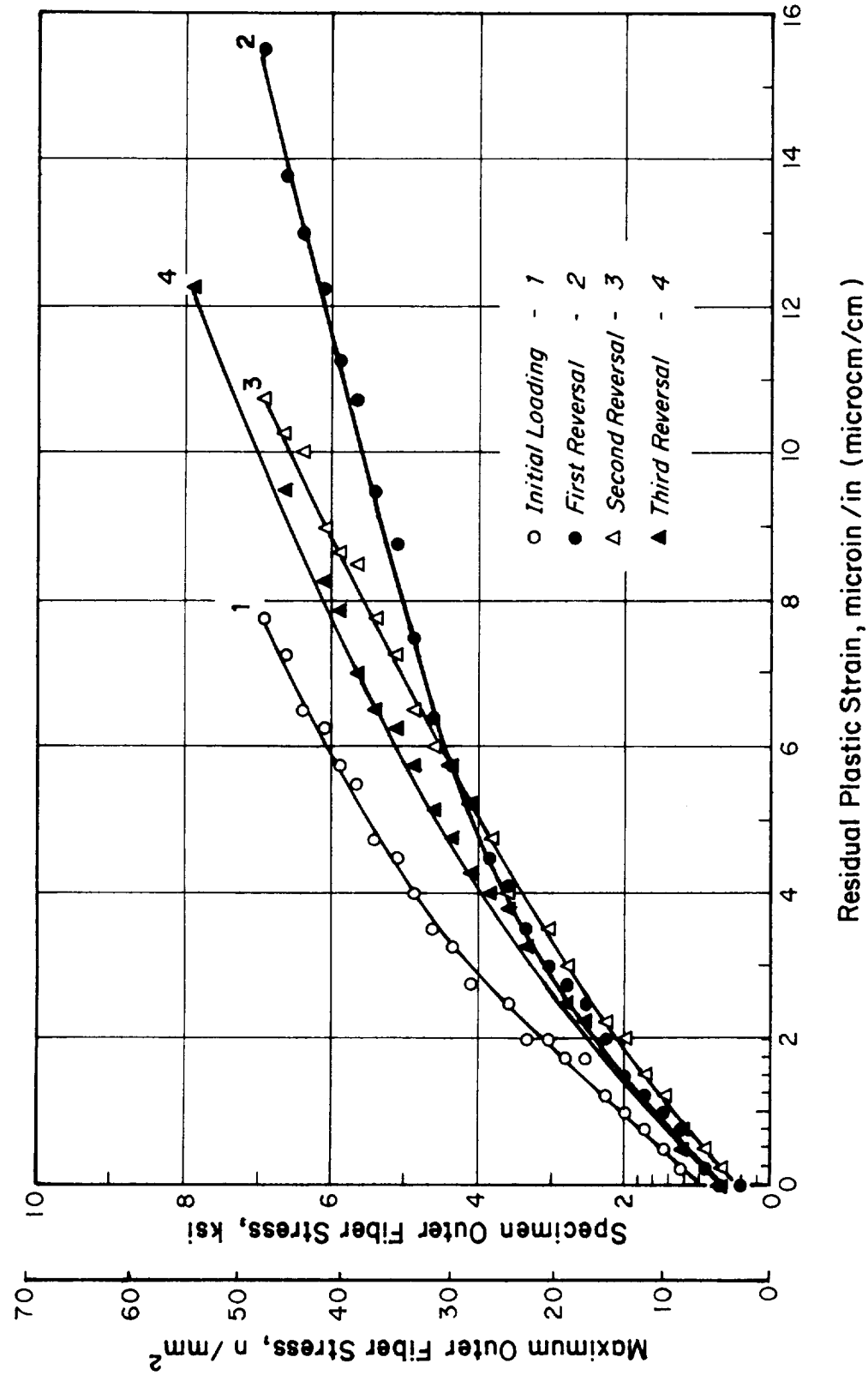

Figure 28 Micro-Bauschinger Effect

Table 3

Precision Elastic Limits of Beryllium*

Material	Treatment	PEL (psi)		PEL (n/mm²)		Reference
		@ 2×10^{-6} strain	@ 10^{-6} strain	@ 2×10^{-6} strain	@ 10^{-6} strain	
Hot Pressed QMV	Chemically polished	10,000	--	68.9	--	2
Hot Pressed QMV	Chem. Pol. - Ann. 2 hrs. @ 1472F (1073K)	3000-3600	--	20.7-24.8	--	2
Hot Pressed QMV	Chem. Pol. - Ann. 2 hrs. @ 2012F (1373K)	2600-3500	--	17.9-24.0	--	2
Hot Pressed QMV	Chem. Pol. - Ann. 18 hrs. @ 2012F (1373K)	2,600	--	17.9	--	2
Hot Pressed QMV	As Machined	6,500	--	44.8	--	3
Hot Pressed QMV	Mach. - 0.0105 in. removed by chem. etch	10,000	--	68.9	--	3
Hot Pressed	As pressed	5,600	4,000	38.5	27.6	4
Hot Pressed	Forged powder	5,600	5,200	38.5	35.8	4
Hot Pressed	Forged (highly deformed)	10,000	7,600	68.9	52.3	4
Hot Pressed	Instrument grade	8,500	7,000	58.5	48.2	4
Hot Pressed	-200 mesh, 100% virgin	--	2,200	--	15.2	5
Hot Pressed	-200 mesh, std. production grade	--	2,663	--	18.4	5
Hot Pressed	-200 mesh, 60% recycle and 40% virgin	--	4,100	--	28.3	5
Hot Pressed	-200 mesh, 100% recycle	--	4,300	--	29.5	5
Hot Pressed	Subsieve, 100% virgin	--	4,333	--	29.9	5
Hot Pressed	-325, 100% virgin	--	6,500	--	44.8	5
Hot Pressed	-200, dispersed iron alloy	--	6,833	--	47.0	5
Hot Pressed	Subsieve, 100% recycle	--	11,167	--	77.0	5

*Although not verified in all cases, it is assumed that most results were obtained in axial tensile tests.

It is apparent that reported results vary considerably and these variations may be due to testing procedures or may represent actual variations in material behavior with the manufacturing and processing procedures used.

The results of ARA bend tests show a precision elastic limit of 1300 to 2010 psi (8.95 to 13.85 n/mm^2) at 10^{-6} strain and 2000 to 3050 psi (13.8 to 21 n/mm^2) at 2×10^{-6} strain. These values are lower than most of the reported data. Further check tests are in process at ARA.

As a result of developments in instrument grade beryllium it is now possible to obtain material such as Bendix 450 Grade D to a specified precision elastic limit of 9000 psi (62.0 n/mm^2) minimum. Bend test data will be obtained by ARA on this alloy in the manner reported above, on a sample now being machined. The material certification on this sample of beryllium being tested indicated a PEL of 11,400 psi (78.5 n/mm^2).

Taking into account the general behavior of beryllium at low stress levels and its potentially low precision elastic limits, consideration should still be given to other candidate materials for the production of the gyro. One such material on which there has been considerable experience is the bearing steel 52100 but only limited data are available on its micromechanical properties. Tests are now in process at ARA to measure the precision elastic limit and other microstrain behavior of this steel for comparison with beryllium. Precision elastic limits of hardened tool steel in general are quite high and a high value is anticipated for 52100. The behavior of high purity alumina and beryllia needs further study since limited data indicate that the PEL of these materials is equal to the ultimate tensile strength, 25,000 and 20,000 psi (172 and 138 n/mm^2) respectively (Ref. 9).

CONCLUSIONS

A. Shaft

1. Shaft deformations are reliably predictable using elementary beam theory.
2. Axial forces should not affect significantly the shaft deflections due to moment loading.
3. Localized stresses are to be anticipated at the changes in shaft cross section.

B. Fork

1. The current fork would be satisfactory for the static equivalent of 100g shock.
2. An efficient fork design for shock resistance and temperature fields could be achieved with wide, thin fork arms. However, the excessively low PEL of S-100 beryllium would require unrealistic fork dimensions.

C. Temperature

1. The currently contemplated startup could induce a shaft peak temperature as high as 180 F (355 K), according to a highly simplified transient thermal analysis.
2. Since the transient analysis approaches the previously obtained steady state temperatures at long times, the method may be of value in selecting alternate startup power/time functions.

D. Materials

1. The ECL 450 Grade A (S-100) beryllium tested at ARA exhibited a PEL between 1300 and 2000 psi (9 and 13.8 n/mm^2) strain.
2. Load reversal did not influence the microplastic behavior significantly.
3. Room temperature creep can occur at low stress levels.
4. The ECL Grade D (I-400) high PEL beryllium has a specified PEL of 9000 psi (62 n/mm^2), which is more than four times that of beryllium (ECL 450 Grade A) tested at ARA.
5. It is anticipated that 52100 steel will have a PEL in excess of that for beryllium by approximately an order of magnitude.

APPENDIX

Data on Beryllium Used in Microplasticity Tests

Material: QMV Beryllium Rod, 3/8" (95 mm) diameter

Supplier: The Brush Beryllium Co.

Specification: Bendix Spec. 450 A, Grade A

Density: 1.84 gm/cc

Chemical Analysis: (Wt. %)

Be	99.2	Mg	0.01
BeO	0.83	Si	0.02
C	0.09	Mn	0.01
Fe	0.07	Each Other Metallic Impurity	0.04
Al	0.07		

Mechanical Properties (Reported by Supplier):

	σ_{tu} psi	σ_{tu} n/mm^2	σ_{ty}(0.2) psi	σ_{ty}(0.02) n/mm^2	ϵ % in 2" (50.8 mm)
Longitudinal	43,800	302	29,900	206	2
Transverse	48,900	337	29,500	204	3

REFERENCES

1. Becker, H., Hultin, R., Kyle, P. E., "Photomechanical Investigation of Structural Behavior of Gyroscope Components," Allied Research Associates, Inc., Report No. ARA-F-284, Task I, July 9, 1965.
2. Timoshenko and Gere, "Theory of Elastic Stability," McGraw-Hill Book Company, 1961.
3. Wang, "Applied Elasticity," McGraw-Hill Book Company, 1953.
4. Carnahan, R. D., "Microplasticity," SSD-TDR-64-124, Ballistic Systems and Space Systems Division, Air Force Systems Command, Los Angeles Air Force Station, Los Angeles, Calif., July 15, 1964.
5. Bonfield, W. and Li, C. H., "Dislocation Configurations and the Microstrain of Polycrystalline Beryllium," Acta Metallurgica, Vol. II, pp. 585-590, June 1963.
6. Bonfield, W., Sartell, J. A. and Li, C. H, "The Effect of Surface Condition on the Microstrain of Beryllium," Trans. of the Metallurgical Society of AIME, Vol. 227, pp. 669-673, June 1963.
7. Jennings, C. G., Colteryahn, L. E., and Bester, M. H., "What to Consider When Applying Beryllium," Metal Progress, pp. 104-108, May 1965.
8. Hughel, T. J., "An Investigation of the Precision Mechanical Properties of Several Types of Beryllium," General Motors Lab Report MR-120, April 24, 1960. (See also DMIC Memorandum 189, March 19, 1964)
9. Jennings, C. and Brenner, H. S., "Precision Elastic Limit," Machine Design, pp. 163-165, April 15, 1965.